University of Alberta

Multi-Modal Registration of Maxillodental CBCT and Photogrammetry Data over Time

by

Niousha Bolandzadeh-Fasaie

A thesis submitted to the Faculty of Graduate Studies and Research
in partial fulfillment of the requirements for the degree of

Master of Science

Department of Computing Science

Spring 2011
Edmonton, Alberta

Examining Committee

Pierre Boulanger, Department of Computing Science

Walter F. Bischof, Department of Computing Science

Nilanjan Ray, Department of Computing Science

Carlos Flores-Mir, Department of Dentistry

To my beloved mother
And my precious grandparents
For their open-mindedness, supports, motivations, patience, and love.

Abstract

This thesis aims at introducing a methodology for clinical evaluation of orthodontic treatments using three-dimensional dento-maxillofacial images. Since complementary information is achieved by integrating multiple modalities, cone-beam computed tomography (CBCT) and stereophotogrammetry technologies are used to develop a methodology for tracking bone and facial skin variations over time.

Our proposed methodology consists of a two-phase registration procedure. In the first phase, the multimodal images are registered using an extrinsic landmark-based registration followed by a robust Iterative Closest Points (ICP) method. In the second phase, by utilizing specific anatomical landmarks, single modal images of the skull and the mandible are registered over time using an intrinsic landmark-based registration method followed by the robust ICP algorithm. The results of registrations show that the signed error distribution of both mandible and skull registrations follow a normal distribution while all the errors fall within the CBCT precision range.

Acknowledgements

This thesis is the result of the amazing two year experience at the University of Alberta. Behind this endeavor stand many individuals who guided, inspired, and helped me through my Master's studies, and made this thesis possible.

I owe my deepest gratitude to my supervisors, Prof. Pierre Boulanger and Prof. Walter Bischof for their continuous guidance and support throughout my Master's program. Thank you Pierre for providing me the great opportunity of working on the multi-disciplinary area of medical imaging, and also for your invaluable insights, constructive feedbacks, motivation and encouragement on this thesis. Pierre, your support in every aspect of my graduate life, from guiding me to learn imaging algorithms to making discussions about world's cultures and histories, was beyond a supervisor's duty. I would like to deeply thank you for believing in me in this two-year journey. And thank you Walter, for providing a great support at the very first days of settling in Edmonton. I have also been very fortunate for having you in the statistical analysis section of my thesis, and thank you for teaching me communication and time management throughout my Master's degree.

I would extend my sincere acknowledgement to my committee members, Dr. Carlos Flores-Mir and Dr. Nilanjan Ray, for taking the time to read my thesis, and for providing me with great comments on both medical and algorithmic aspects of it. Thank you Carlos for your continuous support and insightful advices on my thesis, and your constructive revisions on our published paper. Your dedications, from your email responses to patiently describing me the orthodontic aspects of my thesis, are truly appreciated.

I would also like to gratefully acknowledge the wonderful professors at the department of Computing Science, Dr. Denilson Barbosa, Dr. Joerg Sander, and Dr.

Russel Greiner for their time, and continuous support, motivation, and inspiration throughout this journey. I would also like to thank my current PhD supervisor, Dr. Teresa Liu-Ambrose for her understanding, patience, and encouragement in my three months of joint Master-PhD program.

Working with all the lab members in the Advanced Man-Machine Interfaces laboratory (AMMI) was a great experience for me. I specifically would like to thank Maria Kazakevich, Victor Ochoa Mayorga, Xingdong Yang, Biao She, Xiaozhou Zhou, and Emily Wu. Thank you Maria for your valuable friendship, and for standing by my side in the best and worst days of my life in Edmonton. Thank you the senior lab members, Victor and Xingdong, for your continuous support, and for answering my questions patiently. A sincere thank you to Biao, Xiaozhou, and Emily for your care and encouragement, for bringing happiness to the lab, and for your positive attitude. Without you, I would have never been able to smoothly adjust to my new life. I would also like to thank Mrs. Edith Drummond for all of her support during my two year program at the University of Alberta.

I would like to extend my gratitude to my Persian friends at the Computing Science department who supported and helped me in the past two years of my studies; Reihaneh Rabbani, Reza Sadoddin, Parisa Mosayebi, Mansoureh Takaffoli, Amir-massoud Farahmand, Mohammad Shafiei, Yavar Naddaf, Shahin Jabbari, Shahab Jabbari, AmirAli Sharifi, and Yasin Abbasi. Thank you Reihaneh for your great support from the first days in Edmonton to the last ones, for standing beside me on the worst days of the first semester, for being the best classmate (although sleeping during the seminars!), for staying beside me late in the middle of the nights for delivering the assignments, and for everything else you did throughout these two years. Thank you Reza for taking the time to read my writings, for providing effective feedbacks to my concerns, for discussing controversial issues with me, and for always motivating me to my goals (except continuing my studies to PhD!). Thank you Parisa for believing in me, and thank you for being open-minded, and providing directions to my happiness. Thank you Mansoureh for your great helps in the first weeks of living in Edmonton. Thank you Amir-massoud for showing me the world of books, and teaching me the “let it go”. Thank you Mohammad and Shahin for

your energy and coolness! Thank you Yavar for your friendship. Thank you Shahab for caring about me. Thank you AmirAli for your great comments specifically on my thesis seminar. Thank you Yasin for patiently answering my statistic question.

I owe my special thanks to Pirooz Chubak for whatever he did for me during my studies. Thank you Pirooz for always picking me up when I fall, and thank you for your endless supports in every aspect of my studies and life. Thank you for taking so much time on my writings, for guiding me to solve computational problems, for giving me constructive feedbacks, and for believing in me throughout my graduate life. Thank you for being my inspiration, and for encouraging me to take the risks for following what makes me happy. Thank you for being there for me, and making me happy everyday.

Finally, I would like to thank my beloved mother, grandmother and grandfather, whose open-mindedness, intelligence, inspiration, support, patience, and love made me who I am today. To them I dedicate this thesis.

Table of Contents

List of Tables

List of Figures

Chapter 1

Introduction

Medical Imaging refers to the science of probing structures and functions of the human body, through medical images obtained from various imaging modalities. One of the current important issues in medical imaging is the ability to track and evaluate patients' treatment in 3D over time (also called 4D tracking), through various imaging modalities (MRI, CT, and photogrammetry) obtained before and after the treatment. The information obtained from this process may help with developing better treatments and patient outcomes. This study aims at introducing a methodology for tracking bone and skin variations of the human head over a long period of time, after an orthodontic treatment has been performed. Our proposed tracking system is shown to capture tissue variations accurately for several subjects and over a one-year period of time.

Various imaging modalities have been employed in the field of dentistry. Traditionally, the structures of teeth and jaws have been evaluated by using two dimensional images obtained from projecting X-ray sources to the patients' heads. Cephalometric and panoramic images were for decades the most frequently used modalities by dentists. Although the amount of X-ray radiated to the patients' heads were safe, there were some limitations [24] that prevented the dentists from accurately measuring the anatomy of the patients. These limitations are superposition of anatomical structures and distortions due to hardware limitations in x-ray imaging systems.

During the past two decades, three dimensional (3D) imaging and modeling have brought the "Anatomic Truth" [25] to the field of dentistry. More specifi-

cally, three dimensional images do not suffer from projection or superposition of structures that lead to misrepresentation of the anatomy [6, 61]. Among the imaging systems used in dentistry, Cone-Beam Computed Tomography (CBCT) is used to represent and measure the full anatomy of the head including skull, teeth, and mandible.

Recent advances in the field of CT imaging have led to the development of Cone Beam Computed Tomography (CBCT) systems, which use a cone shaped X-ray beam to construct 3D images of the patients. In comparison to conventional CT, patients using CBCT are exposed to lower X-ray dosages, around 100Sv which is only 1% of the conventional medical CT exposure. This technology produces accurate images of bony structures of the maxillodental areas which have widespread applications in implantology [4], mandibular skeletal corrections [11], and maxillofacial morphology [48]. As investigated by [46, 38, 33], the measurements obtained from CBCT images are of high accuracy for maxillodental applications.

Although images obtained from a single modality, such as CBCT, may suffice to solve some clinical dental issues, in more general cases, dentist must deal with problems relating to different body tissues. Hence, as discussed in [5], it is essential to utilize other imaging modalities in order to get complementary information to capture a complete 3D model of the maxillodental structures and tissues. As a result, adding skin surface information using stereo-photogrammetry to the skeletal data taken from CBCT may be essential. As an example, three-dimensional images of the skin along with color information may give surgeons an assessment on how swellings evolve during patient recovery. The ability to fuse the two imaging modalities enables interactive surgical planning, leading to objective and accurate tracking of surgery outcomes. Many studies such as [32, 3, 63, 49, 51, 34, 31] have shown the reliability of digital measurements using stereo-photogrammetry, and therefore have recommended its use as an accurate surface imaging system for clinical applications.

During the past decade, many studies have been conducted on fusing CBCT and photogrammetry including evaluating their accuracies [46, 38, 3, 18, 49, 51, 63] and the ability to track patients over time [11]. The most relevant study is a pilot study

in [35] on the registration of skull and face data, both extracted from CT. This research demonstrated the importance of 4D image analysis in orthodontics and dentistry. However, to the best of our knowledge, no research has been conducted capable of tracking soft and hard tissues simultaneously during an orthodontic treatment for long periods of time (greater than six months).

1.1 Thesis Contributions

Our proposed tracking methodology includes two registration phases. The first phase consists of registering the CBCT and photogrammetry data at each patient's visit, using an extrinsic landmark-based registration technique. The second phase consists of registering the fused CBCT and photogrammetry data performed at each visit over a long period of time (more than six months), using feature points on the patient's skull and mandible since fixed external targets are impossible to use in this case. One can see in Figure 1.1 an illustration of the proposed image registration process:

1. Data Acquisition

   The first step consists of acquiring almost simultaneously the bony structures of the head using CBCT and face surface structures using a 3dMD stereo-photogrammetry system. Before the acquisition process, the patient is asked to wear a target-band on the forehead composed of six titanium spheres, which can be imaged in both modalities without any problems. This process is explained in Section 5.1.

2. Pre-Processing

   In the second step, which is discussed in Section 5.2, the 3D geometry of the bony structures is extracted from the CBCT using the well-known Marching Cubes algorithm. This technique extracts a polygonal model from tracking an iso-density value corresponding to bone. In a similar way, a polygonal model of the patient's face is extracted by solving the correspondence problem between the four cameras looking at the patients. The face color taken by two high-resolution color cameras is then added onto the face geometry.

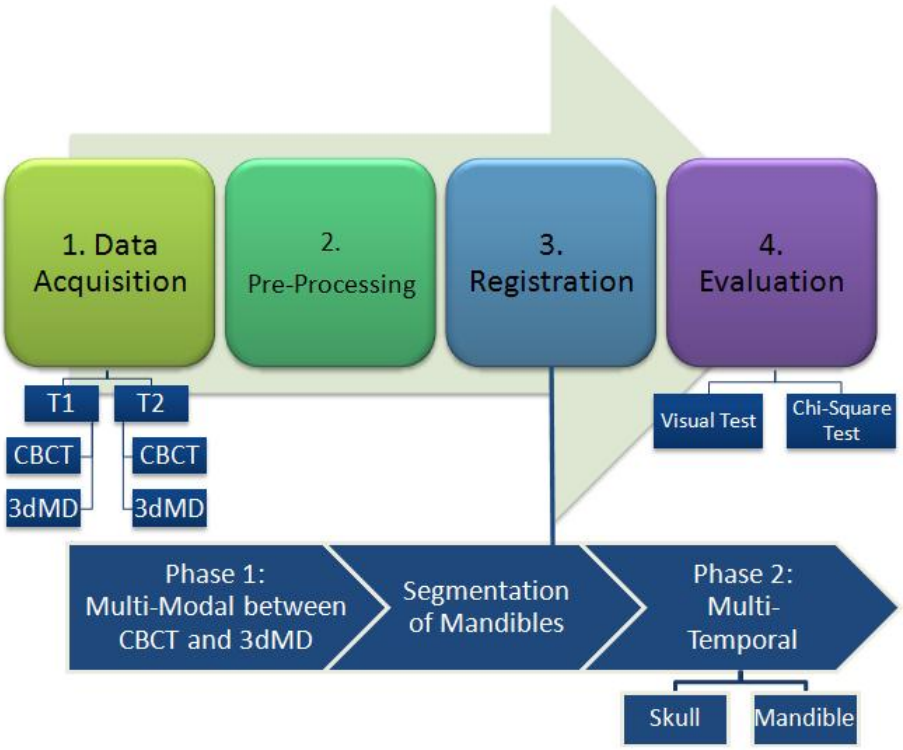

Figure 1.1: Procedure of complete registration of CBCT and 3dMD maxillodental data over time.

Once 3D polygonal models of the bone and the face are extracted, a filtering process removes adaptively (based on curvature) redundant points and deals with outliers.

3. Registration

   The third step involves a two phases registration process:

   Phase1 : The first phase consists of extracting the targets in both modalities and then registering them using a 3D rigid registration algorithm. The two geometric models (skull and face) are then registered in the same coordinate systems and saved as a unique polygonal shell that will be used as one entity. This phase of registration procedure is described in Section 5.3.1.

   Phase2 : The second phase, as explained in Section 5.3.2, uses intrinsic landmarks on the skulls geometry at times T_1 and T_2 to initialize the registration. Based on this registration, an automatic robust registration algorithm is applied. The two shells containing the registered bone-face 3D models at each

time step are then transformed in the same coordinate system. The assumption here is that most of the upper skull will not have change during the measuring periods.

Since the mandibles move independently of the upper skull and therefore should be registered separately, the same registration procedure as explained in Section 5.3.2, with specific extrinsic landmarks was performed on the mandibles after their segmentation from the upper skull. It was again assumed that most of the mandible will not have change during the measuring periods.

4. Evaluation

   The last step discussed in Section 5.5.3 computes the difference between the corresponding points in two time steps and displays them using color codes. We also determine the validity of our proposed registration process by using a goodness of fit test to show that all the skull and the mandible results, after trimming, follow a normal distribution with the significance level of 95%, indicating that there is no systematic bias due to our methodology.

1.2 Thesis Organization

This thesis is organized as following:

Chapter 2: In Chapter 2, we explain hard tissue acquisition using X-ray modality. We describe the capabilities of this modality and how precise the measurements are. We also introduce the link between imaging quality and dose for different X-ray dental imaging modalities. In Sections 2.3.1 and 2.3.3 we will describe the working principles of two tomographic X-ray imaging modalities: Conventional Computed Tomography (CT) and Cone-Beam Computed Tomography (CBCT). We will describe various algorithms for back-projection as it relates to image reconstruction and the extraction of geometry through the Marching Cubes algorithm. In Section 2.5, the CBCT system used for this study is described.

Chapter 3: In Chapter 3, we introduce different modalities used for surface acquisition, and explain their accuracies and capabilities. We then discuss how pho-

togrammetry can be used for skin acquisition. Two challenges in photogrammetry, i.e correspondence problem and triangulation, are described in Section 3.3. The last section describes the 3dMD system used in this study.

Chapter 4: In Chapter 4, the registration problem is defined, and the role of registration in this project is explained. Then two registration methods are presented,

1. Landmark-based methods, and
2. Template-based iterative closest point algorithm.

The chapter concludes by introducing skull and mandible landmark systems used in literature for registration, and a selection of landmarks used in this study.

Chapter 5: In Chapter 5, we will first explain the data acquisition and pre-processing techniques used. Then, the two phases of registration procedures are explained. Section 5.3.1 introduces a methodology for multi-modal registration of CBCT and 3dMD, and Sections 5.3.2 and 5.3.2 explain the multi-temporal registrations for the skull and the mandible respectively. Then we explain the goodness-of-fit tests, which represent how well our registered data are following the normal distribution. The results of our normality tests are shown in Sections 5.5.3 for both skull and mandible registrations.

Chapter 6: We conclude and describe future avenues of the research in Chapter 6.

Chapter 2

Hard Tissue Acquisition: X-Ray Computed Tomography

2.1 Introduction to Computed Tomography: Reliability of the Measurements

Maxillofacial treatment refers to the field that treats the entire anatomical structures of the head: skull, face, mouth, jaws, and related areas. Three-dimensional visualization and imaging techniques have been used in this field for diagnosis, preoperative planning, and surgical navigation. Multiple imaging modalities are now used to construct 3D models of different parts of the head. Bony structures can be measured in high definition from cone-beam computed tomography (CBCT) scanners, soft tissues like muscles from MRI, and skin from stereo-photogrammetry. In this chapter, we will study how CBCT can be used to extract exact geometric models of the bony structures of the head.

CBCT technology has gone through a rapid growth since its introduction in 2000. Improved acquisition speed, resolution, and lower X-ray dosage have made CBCT the primary choice for maxillofacial applications.

Many studies have investigated the accuracy and repeatability of measurements performed on CBCT images. Moerenhout et al. [46] assessed the accuracy of measurements on a phantom's 3D face surface obtained from a CBCT scanner, and compared them with higher precision measurements from optical laser scans. Their study demonstrated the reliability of distance measurements between facial landmarks with a maximal deviation of 1.9mm. Howe et al. [28] also took advantage of

CBCT to perform small measurements on bony structures. They compared calliper measurements with the CBCT measurements for 414 data points on the skull, and reported a standard deviation of these measurements to be on average 1.1mm.

Moreover, Lascala et al. [38] investigated the accuracy of linear measurements in CBCT images of head structures. They collected 13 real linear measurements out of 13 chosen anatomical landmarks, and compared them with those taken from CBCT scans. Their results showed that the real measurements are always larger than CBCT ones, but the differences are only significant for internal skull measurements. They demonstrated that CBCT is a highly precise scanning system for dento-maxillofacial applications.

In this chapter, the theory and physics behind X-ray imaging will be discussed. Then two X-ray Computed Tomography (CT) modalities known as conventional CT and cone-beam CT will be introduced, and the advantages and disadvantages of each will be discussed. In Section 2.4, a generic CT scanner will be described from the viewpoint of data acquisition, image reconstruction, and image segmentation. In the last section, the structure of the NewTom CBCT machine from which all the data is obtained, and the process of image acquisition will be discussed.

2.2 Fundamentals of X-Ray Imaging

X-ray is an electromagnetic radiation that can be viewed as photon particles, with energies ranging between 120 electron-Volts (eV) to 120 KeV. They are categorized to be soft or hard depending on their energy. Hard X-rays, which have energy levels between 12 to 120 KeV can penetrate solid materials, and therefore can be utilized to image the inside of objects, such as body tissues. As discussed in [58], when an X-ray beam is radiated into the body, the photons can either be absorbed by the other atoms, or transformed into an electron-positron pair. This process makes the radiation attenuated and therefore causes a change in the intensity of the beam. One can see the attenuation process in Equation 2.1. The intensity of the outgoing beam $I_{outgoing}$ is related to the incoming intensity $I_{incoming}$ by the absorption of the material (μ), and the width $(x_2 - x_1)$ of the material traversed, as depicted in

Figure 2.1: The outgoing X-ray intensity is related to the incoming intensity, material of the tissue, and the width of the medium.

Figure 2.1:

$$I_{outgoing} = I_{incoming}\, e^{-\mu*(x_2-x_1)}. \tag{2.1}$$

Since most tissues are not homogeneous, the linear attenuation coefficient (μ) changes from one point to another. Therefore, Equation 2.1 for nonhomogeneous mediums should be re-written as follows:

$$I_{outgoing} = I_{incoming}\, e^{-\int_{x_1}^{x_2} \mu(x)dx}.$$

The outgoing attenuated X-ray beam can then be absorbed and measured by X-ray detectors. The sensitivity and quality of an image can be quantified by the measure of signal to noise ratio (SNR). This measure shows the ratio of the signal power to the unwanted noise power. In the field of imaging, SNR is defined as follows:

$$SNR = \frac{\mu_{signal}}{\sigma_{signal}}$$

where μ_{signal} is the average signal value, and σ_{signal} is the standard deviation of the signal around a neighbourhood. This factor is dependent on the X-ray dose as the detectability of X-ray decreases when the X-ray acquisition dose decreases.

The X-ray dosage needed for performing tissue radiography varies depending on the devices used. Even low doses might be sufficient to damage or modify cells. If the repairing mechanisms of the human body fail, and the process of irradiated cells' fixation does not work well, then cancer or genetic changes can happen [58]. That is the main reason for physicians to check the risks of radiological devices,

Table 2.1: Comparison of effective radiation dose for orthodontic X-ray technologies vs. their equivalent natural radiation. Courtesy of James Mah, DDS, MSc, X-ray Imaging and Oral Healthcare, 2006 [42].

Examination	Effective Radiation Dose (mSv)	Equivalent Natural Radiation
Panoramic	3 to 11	half to one day
Cephalogram	5 to 7	half to one day
Occlusal Film	5	half day
Bite Wing	1 to 4	half day
Full Mouth Series	30 to 170	4 to 21 days
TMJ Series	20 to 30	3 to 4 days
CBCT Exam	40 to 135	4 to 17 days
Medical CT	8000	1000 days

and they have to decide about an imaging system that not only can image the desired tissues, but keeps the dosage as low as possible for the patient. This radiation protection is referred to as keeping the exposure "ALARA (As Low As Reasonably Achievable)" [6]. Table 2.1 [42] shows the effective radiation doses for many orthodontic X-ray modalities, and compares each with the equivalent natural background radiation. As one can observe from the table, the decision to use some of these radiological modalities may have a huge effect on the radiation exposure to the patient.

2.3 Computed Tomography Modalities

2.3.1 Conventional Computed Tomography (CT)

Tomography comes from the Greek word "Tomos" which means sectioning or slicing. Computed Tomography known as CT is a tomography-based imaging method that employs computer processing and mathematical analysis of two dimensional images (cross-sections) taken by the X-ray CT scanners to generate three dimensional images of the objects. This technology measures X-ray photons transmitted through the subject's organ along a single projection line, and presents the X-ray attenuation properties of the body [58] quantified as Hounsfield numbers.

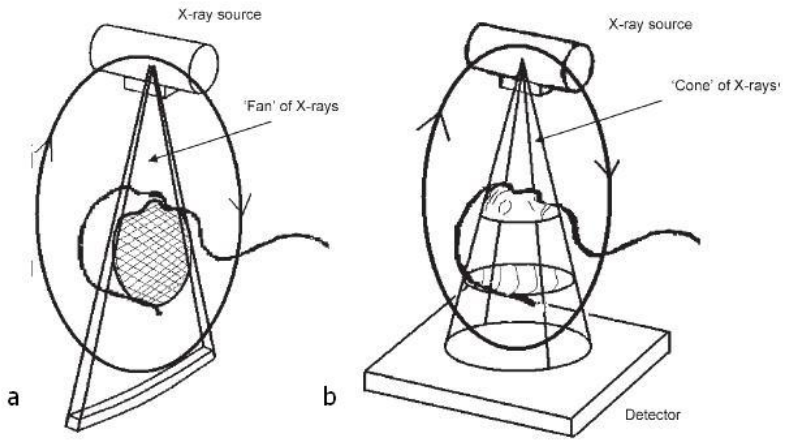

Figure 2.2: The difference of scanning techniques in a: CT and b: CBCT. From Arun Singh, Imaging Sciences, Hatfield PA,USA [54].

Conventional CT scanners consist of an X-ray generator (tube) and an X-ray detector, which are mounted on a CT scanner device, on the opposite side of each other, as shown in Figure 2.2.a. This source/detector assembly rotates as a unit around the object, and takes sequential scans at fixed angular increments. A cross-section or slice can be produced when the assembly accomplishes a 360 degrees rotation. During a complete rotation, the detector receives numerous snapshots of the X-ray beam from different angles. After restoring the data for cross-section reconstruction, the patient table moves forward for acquiring other slices. These slices will be later used to build a three dimensional model by stacking them on top of each other.

2.3.2 Conventional CT versus Cone-Beam CT

The high dosage of radiation in conventional CT scanners is a result of separate X-ray exposure for each slice. However, advances in Computed Tomography technology have led to Cone-Beam Computed Tomography (CBCT), which reduces the exposure to only one rotation of the X-ray generator-detector assembly, reducing radiation risks, acquisition time, effects of patients movements, and image distortion [53].

Some CBCT devices are also capable of limiting the X-ray exposure to the area of interest, hence limiting radiation to organs that do not need to be imaged. The

CBCT X-ray generator is made of smaller and less costly materials in comparison to conventional CT scanners [59].

2.3.3 Cone-Beam Computed Tomography (CBCT)

CBCT utilizes cone shaped rather than fan shaped X-ray beams to provide volumetric structures of craniofacial regions. This technology has been optimized for dento-maxillofacial assessments due to its high accuracy in these areas [46].

In CBCT, the generator-detector assembly is constructed with a cone shaped X-ray generator, as well as a two dimensional (2D) detector array mounted on opposite side of each other, as depicted in Figure 2.2.b. With only one rotation of the assembly, the detector detects the attenuated X-rays received by the subject and is able to reconstruct multiple slices in one rotation. This capability, in comparison to conventional CT scanners, helps to reduce scan time and therefore artefacts resulting from longer scanning times. In addition, as one can observe in Table 2.1, the effective radiation dose in CBCT systems is only 1 % of that in conventional CT scanners.

2.4 Mechanism of Computed Tomography Scanners

2.4.1 Data Acquisition

As described earlier, the detector receives the beams from different angles. Figure 2.3 shows the distribution of x-ray beams over the object at an angle θ. Projecting the beams on X and Y axis gives us the new r and s coordinates:

$$\begin{bmatrix} \text{r} \\ \text{s} \end{bmatrix} = \begin{bmatrix} cos\theta & sin\theta \\ -sin\theta & cos\theta \end{bmatrix} \begin{bmatrix} x \\ y \end{bmatrix}$$

$$\Rightarrow x = r.cos\theta - s.sin\theta\cdot$$

$$y = r.sin\theta + s.cos\theta\cdot$$

Using the intensity attenuation Equation 2.1, one can represent the imaging process as:

$$I_\theta(r) = I_0.e^{-\int_{-\infty}^{+\infty} \mu(r.cos\theta - s.sin\theta, r.sin\theta + s.cos\theta)ds}.$$

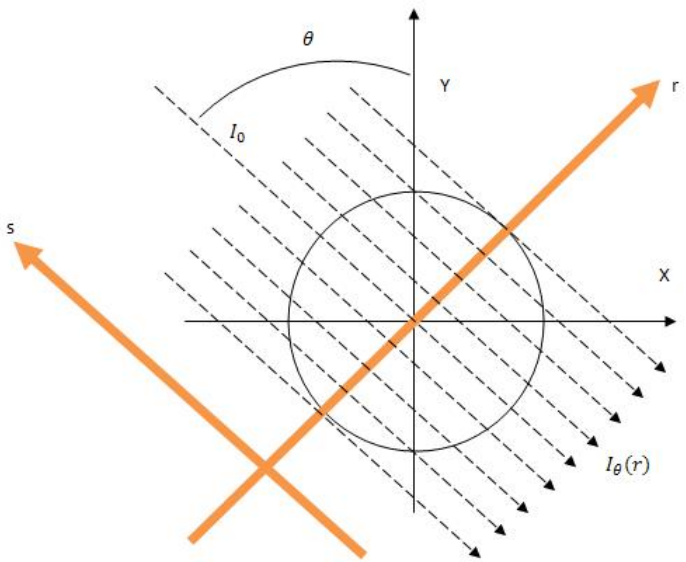

Figure 2.3: X-ray beam attenuation. Courtesy of Paul Suetens, Fundamentals of Medical Imaging, 2009 [58].

Taking the logarithm on both sides:

$$\ln I_\theta(r) = \ln I_0 . e^{-\int_{-\infty}^{+\infty} \mu(r.cos\theta - s.sin\theta, r.sin\theta + s.cos\theta)ds}.$$

By rearranging the terms we have:

$$p_\theta(r) = -\ln \frac{I_\theta(r)}{I_0} = \int_{-\infty}^{+\infty} \mu(r.cos\theta - s.sin\theta, r.sin\theta + s.cos\theta)ds\cdot \qquad (2.2)$$

This integral represents the integral of the density function μ projected on r and s coordinates at different angles θ. The integral is referred to as $p_\theta(r)$ [58]. A sinogram is made by stacking all $p_\theta(r)$s, and making $p(r, \theta)$ which has a sinusoidal shape. This process of making a sinogram is similar to the Radon Transform as described in [58].

2.4.2 Image Reconstruction: Back-projection Algorithm

The data received from each rotation goes under tomographic reconstruction to build a two dimensional cross-sectional image. In this process, each data point is being convolved with the neighbours, and a back-projection algorithm is used to reconstruct the slice. The results can be later used to build the three dimensional model by stacking each slice on top of the other.

The back-projection algorithm is based on Equation 2.2, in which μ is the linear attenuation coefficient that represents the distribution of X-ray intensity inside the irradiated tissue. Having the sinogram $p(r, \theta)$, the back-projection algorithm uses the inverse of Radon Transform to extract the density function μ:

$$\mu(x, y) = \mathcal{R}^{-1}(p(r, \theta))\cdot$$

Finding the density function μ is possible based on the Central Slice Theorem. If we consider $F(k.cos\theta, k.sin\theta)$ as the 2D Fourier Transform of $\mu(x, y)$,

$$F(k.cos\theta, k.sin\theta) = \int_{-\infty}^{+\infty} \int_{-\infty}^{+\infty} \mu(x, y) e^{-2\pi i(k.cos\theta.x + k.sin\theta.y)} dxdy,$$

and $P_\theta(k)$ as 1D Fourier Transform of $P_\theta(r)$,

$$P_\theta(k) = \int_{-\infty}^{+\infty} P_\theta(r) e^{-2\pi i(k.r)} dr,$$

then,

$$P(k, \theta) = F(k.cos\theta, k.sin\theta),$$

where $P(k, \theta)$ is the 2D function of $P_\theta(k)$. Intuitively, the central slice theorem states that the 1D Fourier transform of a Radon transform of a 2D μ function with respect to r, is the 2D Fourier Transform of the μ function. Therefore, the density function μ can be extracted based on the projections $p_\theta(r)$.

The following is the back-projection algorithm:

1. Find the 1D Fourier Transform of all the projections $p_\theta(r)$
   $\mathcal{F}(p_\theta(r)) = P_\theta(k)$

2. Find the 2D function of $P(k, \theta)$
   $P(k, \theta) = F(k.cos\theta, k.sin\theta)$ based on the Central Slice Theorem

3. Find the 2D Fourier Transform of $F(k.cos\theta, k.sin\theta)$
   $\mathcal{F}(F(k.cos\theta, k.sin\theta)) = \mu(x, y)$

2.4.3 Iso-surface Segmentation

CT scan images can either be shown on a film as 2D slices, or they can be presented in 3D on high resolution screens using volume rendering algorithms. In the case

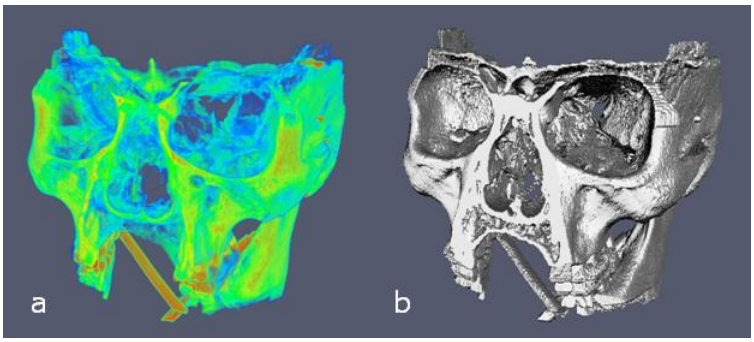

Figure 2.4: The geometry construction of a skull (b), from its volumetric density data (a).

of surface reconstruction for geometric processing, the desired skull volume should be first extracted from the neighbouring tissues. This extraction process is called segmentation. There are various methods for skull segmentation, such as atlas-guided techniques [13] and region growing segmentation methods [45]. However, according to [23], most methods take advantage of threshold criteria in combination with gradient analysis.

The Marching Cubes [40] algorithm is an interactive segmentation that uses user-defined thresholds to produce polygonal triangle meshes of constant density surfaces (iso-surface) from 3D data [16]. As a consequence, different surfaces such as skull and skin can be extracted from a 3D volume density model. Figure 2.4 represents the geometry construction of a skull from its volumetric density data.

Consider the volume as a density function $D(x, y, z)$. In this sense, the extraction algorithm tries to find the surface which satisfies $D(x, y, z) = c$, in which c is a constant [39]. As shown in Figure 2.5, the Marching Cubes algorithm uses the divide-and-conquer method to find the surface in an imaginary cube created from four pixels in a slice combined with four other pixels from the adjacent slice.

This algorithm first makes an imaginary cube around a voxel by taking the eight neighbour locations. Each of these neighbours can be considered as a bit, hence making an eight bit integer. The value of the bits can either be above or below a certain threshold, known as the iso-surface value, therefore making 256 (2^8) possibilities for cubes' configurations. Fifteen out of 256 configurations shown in Figure 2.6 are found to be unique, hence making the total possible surfaces. Then for

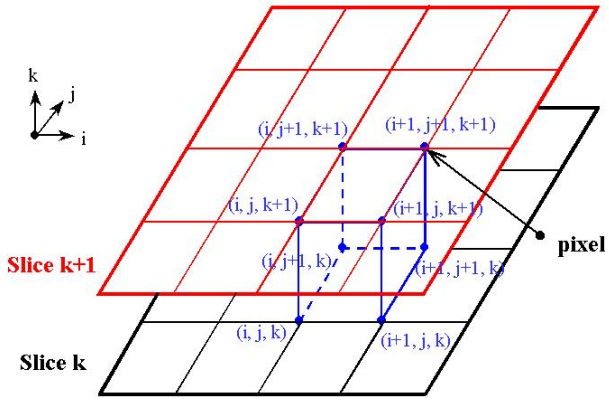

Figure 2.5: The imaginary cube created from eight pixels for Back-projection algorithm.

each configuration, the algorithm replaces the cube with a surface.

As described in [40], the orientation of the surface is calculated by finding the normal vector at a surface point, which can be calculated using gradients at each vertices:

$$G_x(i,j,k) = \frac{D(i+1,j,k) - D(i-1,j,k)}{\Delta x} \tag{2.3}$$

$$G_y(i,j,k) = \frac{D(i,j+1,k) - D(i,j-1,k)}{\Delta y} \tag{2.4}$$

$$G_z(i,j,k) = \frac{D(i,j,k+1) - D(i,j,k-1)}{\Delta z} \tag{2.5}$$

The result is a complete surface representing a specific intensity value. Figure 2.7 shows the 3D surfaces representing different density values for skin and the

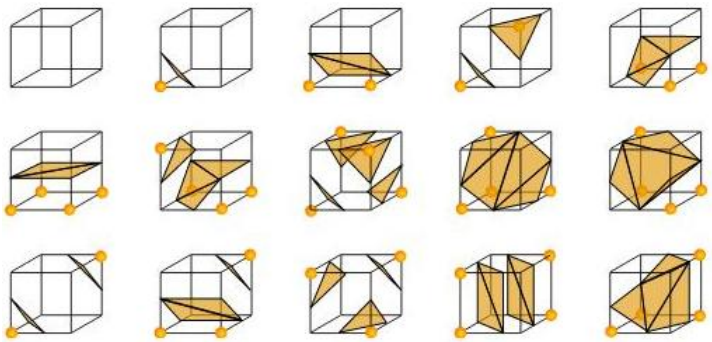

Figure 2.6: 15 unique cube configurations which make the total of 256 possibilities in the Marching Cubes algorithm. Wikipedia, Wikimedia Foundation, Inc.

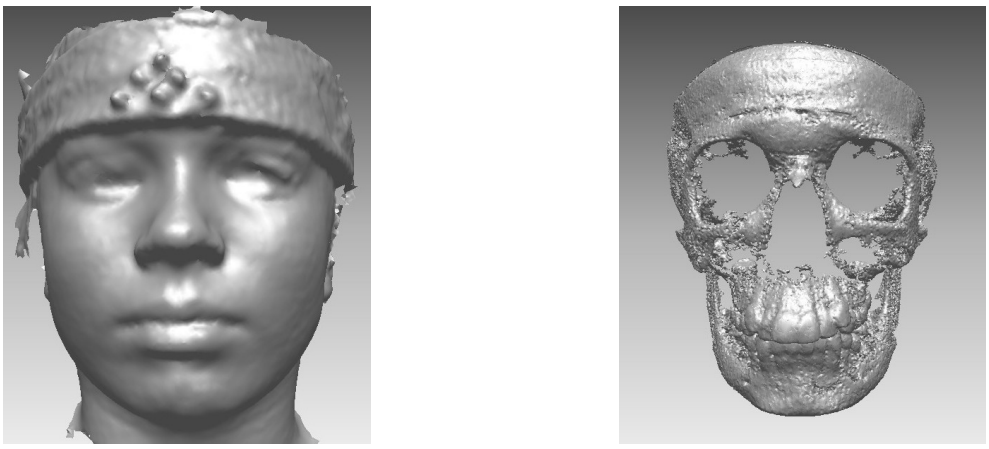

Figure 2.7: 3D surface representing different density values, for skin (left) and skull (right).

skull respectively.

2.5 CBCT System: NewTom QR - DVT 9000

In this thesis, a NewTom QR - DVT 9000 machine (Quantitative Radiology, Verona, Italy) shown in Figure 2.8 was used for hard-tissue acquisition. As discussed in [30], this CBCT system is dedicated for dento-maxillofacial applications, and is composed of the following components.

1. A scanning System : X-ray Source, Bi-dimensional Detector
2. A patient's Table : Table, Laser Pointers
3. A workstation
4. Back-projection and 3D visualization software

The scanning system contains an X-ray source, which produces cone-shaped X-ray beams, and an X-ray bi-dimensional detector. The generator and detector assembly are mounted along a 360 degree arc, and are synchronized with each other by the software to reduce the patient's exposure. During a scanning process, the patient is placed supine on the patient's table, and two laser pointers are used to locate the head at the center of the scan system. Then, the scanning system turns around the subject's head and acquires images. At the end of the 75 seconds

Figure 2.8: NewTom QR - DVT 9000, the first CBCT (Cone-Beam Computed Tomography) imaging system. Courtesy of Boulanger et al. [9].

of scanning time, one axial section of the head is reconstructed and displayed to assure the operator that the data is correct. The patient can then leave the table and be scanned by a stereo-photogrammetry system to capture the geometry of the face. After scanning, the bi-dimensional scan data is transmitted from the detector to the workstation. These raw data are then back-projected to find the attenuation coefficient (μ) of the captured tissues, and the bone surface is reconstructed using a Marching Cubes algorithm set for bone density.

As stated by the manufacturer, the following are the underlined characteristics of QR-DVT 9000 machine:

1. Elevated signal-to-noise ratio (SNR) by utilizing X-ray detector with a high quantum efficiency,

2. Optimizing X-ray beam intensity in relation to subject's head thickness, and

3. Minimizing dosage depending on the image quality requested by the operator.

2.6 Conclusion

In this chapter, we explained hard tissue acquisition using X-ray modalities. We first presented a literature review on the measurements and precisions obtained from

different CBCT studies. These studies have demonstrated that CBCT is a highly precise scanning system for dentomaxillofacial applications. We then described the fundamentals of X-ray imaging, and introduced computed tomography (CT) as an X-ray modality. Then, two CT technologies known as Conventional Computed Tomography (CT) and Cone-Beam Computed Tomography (CBCT) have been introduced, and the mechanism of CT scanners were described. At the end, NewTom scanner, the CBCT system used for this study, was explained.

Complementary to hard tissue information, skin and facial shape information are acquired by stereo-photogrammetry systems. The next chapter is devoted to the shape acquisition modalities, and their mechanisms.

Chapter 3

Human Shape Acquisition: Stereo-Photogrammetry

3.1 Introduction to Surface Acquisition: Reliability of the Measurements

During the last decade, the ability to digitize in 3D the human shape had a great influence on the sciences of morphology, dentistry, and plastic surgery [21]. According to [22], non-invasive and non-ionizing measuring instruments such as laser scanners and stereo-photogrammetric systems have enabled dentists to achieve objective evaluations of treatments supported by quantitative measurements. As discussed in [32], facial growth, craniofacial anomalies, and orthodontic surgeries are the applications that take advantage of these technologies.

Laser scanners can be used for scanning the maxillofacial areas in 3D. Typically, laser scanners project a laser pattern onto the surface to be digitized which is deformed by the relative height variation of the surface relative to the scanner. In many systems, a camera digitizes the deformation of the laser pattern, and by triangulation determines the shape of the surface, producing a dense range map. In many applications, multiple views must be registered and integrated in order to produce a complete model.

There are some attempts in literature to analyze the precision and reliability of laser scanners to digitize the human shape. Coward et al. [15] identified the locations of landmarks on ears and faces, and showed that the variances between repeated measurements of the ears and faces were less than 1mm. Their experiments

suggested that laser scanners are sufficiently precise and reliable for planning facial reconstructions. This technology can also take advantage of recent developments in CAD (Computer Assisted Design) software, where 3D data from laser scanners can be used to construct and print models in 3D, for implants or prostheses developments.

In recent years, stereo-photogrammetry systems were developed to deal with some of the shortfalls of laser scanners. Some systems can provide a colored model of the patient's skin in 3D. The main advantage of this technology over laser scanners is its speed, as it is able to deal with patient motion as acquisition time is less than 100ms. This is a big improvement over laser scanning devices which usually take more than 10 sec to digitize a head. There are many types of 3D photogrammetry devices one can find in literature. A popular system used in different experiments, including this thesis, is the 3dMDface ™system.

Many studies have been conducted on the accuracy of photogrammetry for digitizing the human shape. Aldridge et al. [3] investigated the precision and reproducibility of coordinate data collected from the 3dMD system. Twenty standard anthropometric landmarks mentioned in [18] were identified on the face and ears of 15 subjects whose data were collected two times to test the repeatability. The investigation demonstrated that the measurements produced by the 3dMD system are highly repeatable with an error in sub-millimeter range, making the 3dMD system sufficiently precise for medical applications. Wong et al. [63] also did an experiment on two sets of 3dMD measurements obtained from twenty normal adults, showing the precision on the measurements of 18 distances from 19 standard anthropometric landmarks mentioned in [18]. These experiments, along with similar investigations [49, 51] show that digital measurements are reliable and that the mean absolute difference is less than a millimeter.

In addition to the measurements produced by the 3dMD system, extracting color information from stereo-photogrammetry systems is a valuable asset in different studies. Nestor et al. [47] investigated the role of surface imaging in gender recognition. They extracted contrast information of main features, and compared them with the rest of the face. The results suggest color as a factor for high-level visual

processing. Beside color information, facial morphological differences between males and females have also been investigated. Kau et al. [34] showed that the areas of greatest deviation are in zygomatic and lower jaw, with differences in males being more prominent. These studies show the potential for making useful templates for investigation of maxillofacial anomalies.

Head shape acquisition technologies have great impact on maxillodental surgeries and follow-ups. Kau et al. [31] introduced a method for evaluating the amount of facial swelling after an orthodontic surgery. Their results provide clinical information, both for the patients and the physicians, about the associated soft tissue changes. This methodology is based on 3D surface images of three patients, before and after surgery. Their pre- and post-surgical images were aligned (registered) and compared to evaluate the swellings. This study demonstrated that face swelling can be accurately quantified. The results showed that there was a swelling reduction one month after the surgery, and the facial morphology returned to 90% of its original size by the third month.

Due to its advantages, 3D stereo-photogrammetry is rapidly replacing other technologies as the preferred facial surface acquisition modality [26]. In this chapter, the fundamentals of photogrammetry and stereo-photogrammetry will be presented. Then two important algorithms for correspondence matching and stereo triangulation will be discussed in Section 3.3. We will then describe in detail how the 3dMD system works.

3.2 Photogrammetry

Photogrammetry is the science of measuring objects from their photographs. Many studies have been done on the automation of information retrieval from digital photographs. Many researchers suggest photogrammetry as a non-invasive technique that provides medical staff with basic body shape measurements. However, the usefulness of this technology is limited by the image resolution, and, in the case of medical applications, how one can measure the “anatomic truth”. Studies on the precision of these measurements have been conducted by [3, 32, 49, 51, 63].

They all demonstrated the reproducibility and high accuracy of photogrammetry measurements in the medical field.

One form of photogrammetry with widespread applications in maxillofacial radiology is called stereo-photogrammetry. Since imaging devices convert 3D world to 2D, they cannot project all the details and properties of an object, hence losing key information. Stereo-photogrammetry builds up the lost information again as it computes depth information from two or more images. As stated previously, this information is necessary for constructing the morphology of the face and obtaining objective treatment evaluations supported by quantitative measurements in maxillofacial field.

3.2.1 Stereo-photogrammetry

Stereo-photogrammetry is the science of making 3D measurements from multiple pairs of digitized images. These images are captured simultaneously from multiple static cameras, observing the same scene from different views. This method enables the measurement of the distance. The two fundamental principles used by stereo-photogrammetry are:

1. Correspondence Matching

2. Stereo Triangulation

Since two or more images of the same 3D scene are taken from different angles, the set of points in one image corresponding to the same points in other images should be extracted first. This process of correspondence matching is an area of intense research. When the corresponding points are found in at least two images, they can be used to extract depth information using stereo triangulation.

3.3 Principal Algorithms

3.3.1 Correspondence Problem

The correspondence problem can be stated as follows: Suppose the set P consists of the common points in n photos. Given the geometric point or feature p_1 in $photo_1$,

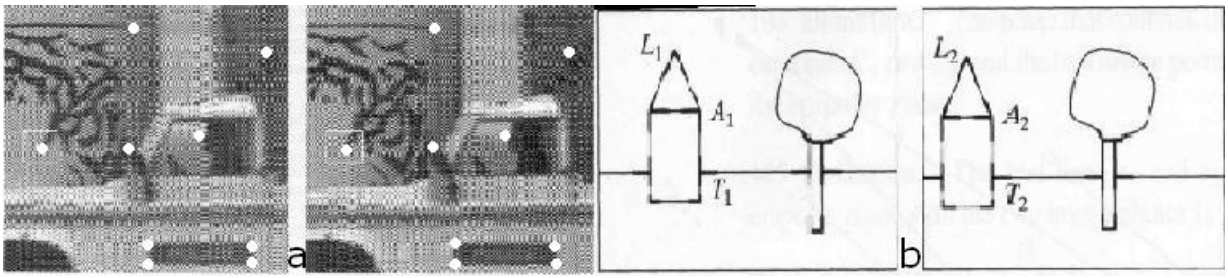

Figure 3.1: Two correspondence matching algorithms. a: Correlation-based method, and b: Feature-based method. Courtesy of George Bebis, University of Nevada, Reno [7].

find the corresponding point or feature p_n in $photo_n$. There are three main classes of correspondence matching algorithms, two of which are shown in Figure 3.1.

1. The *correlation-based method* attempts to find each pixel's disparity which is the difference in coordinates of corresponding points, under the hypothesis that they should have similar intensities. This method conducts a search through $1/2$ window size in each direction, and finds the disparity $d = (d_1, d_2)$ that maximizes cross-correlations of image intensities I_1 and I_2.

```
For each pixel p_n = (i, j) in photo_n do:
  For each disparity d = (d_1, d_2) do:
    c(d_1, d_2) = Σ_{k=-w}^{w} Σ_{l=-w}^{w} I_1(i + k, j + l) I_2(i + k - d_1, j_l - d_2)
  disparity ← argmax_{d_1,d_2} c(d_1, d_2)
```

2. The *feature-based method* tries to solve correspondence by matching sparse set of features in each image. In this sense, this method checks a smaller set of candidates as features than correlation-based methods do. This method uses typical feature properties such as length l, orientation θ, coordinates of midpoint m, and the average intensity i to find the most similar feature on the other image.

   Among the mentioned approaches, the correlation-based method is easier

For each feature $f_n(l, \theta, m, i)$ in $photo_1$ do:

  For each feature in $photo_2$ do:

    $S = \frac{1}{w_0(l_1-l_2)^2 + w_1(\theta_1-\theta_2)^2 + w_2(m_1-m_2)^2 + w_3(i_1-i_2)^2}$

  Feature $\leftarrow argmax_{l2,theta2,m2,i2} S$

to implement, and works well in the presence of texture information. The feature-based method is faster when some features can be extracted from the image. However, structured lighting method can be used beside the mentioned approaches to find a more accurate solution for the correspondence problem.

3. The *structured light projection* technique, as discussed in [37], utilizes structured patterns of lights such as white light or grids that are projected on the subjects. The process of projecting lights is being performed at the same time as the subject is being photographed by calibrated cameras. In this sense, instead of the natural texture of the normal face, the structured light pattern is used to solve the correspondence algorithm. As stated in [7], this method is simplified when the geometry of the projected patterns is known.

When the correspondence problem is solved, a triangulation algorithm is used to infer the coordinates of the corresponding points.

3.3.2 Stereo Triangulation

The required inputs for triangulation are camera positions and the angles they make with an object. As one can see in figure 3.2, two cameras are located in points P and Q, and the object is observable by them. The distance between the cameras is denoted by D. The triangulation algorithm uses these parameters as inputs from which the coordinates of the object is computed. The following calculations determine the distance of the object from the line which connects the two cameras.

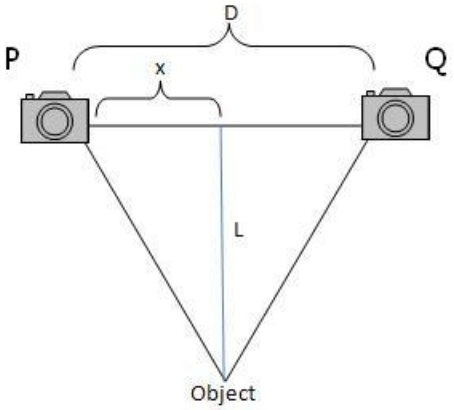

Figure 3.2: Triangulation Principle: Finding the location of an object by the use of two cameras mounted to view the object in different angels. Camera positions and angles they make with the object are known.

$$\begin{aligned} \tan P = \frac{L}{x} &\Rightarrow \frac{1}{\tan P} = \frac{x}{L} \\ \tan Q = \frac{L}{D-x} &\Rightarrow \frac{1}{\tan Q} = \frac{D-x}{L} \\ &\Rightarrow \frac{1}{\tan P} + \frac{1}{\tan Q} = \frac{D}{L}. \end{aligned} \tag{3.1}$$

Equation 3.1 yields the desired object's depth L. This distance can be used for finding the full object coordinates.

$$L = \frac{D}{\frac{1}{\tan P} + \frac{1}{\tan Q}}.$$

After the correspondence matching is determined, and the 3D model is recovered by triangulation, the color information captured from color cameras can be mapped and added to the model. The result is a highly precise 3D colored model, immediately usable for medical applications.

3.4 Photogrammetry System: 3dMDface

The 3dMDface system has been first developed in 1999 and is now in its third generation. This system combines the following techniques to produce a high resolution 3D image of the subjects' shape (mainly the face),

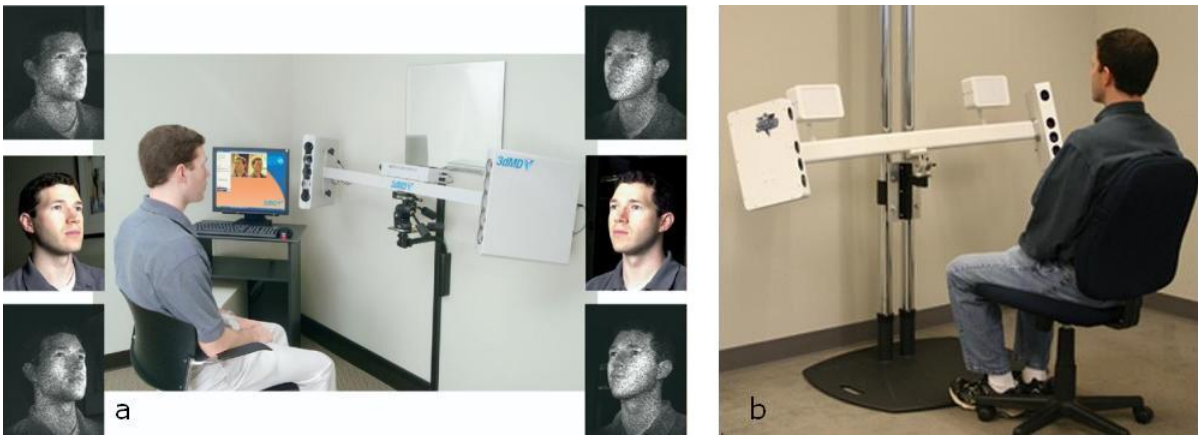

Figure 3.3: 3dMDface device containing six cameras taking shots of the subject. a: Courtesy of Lane et al. [37], b: Courtesy of 3dMD Incorporation [1].

1. Structured Light Projection, and

2. Stereo-Triangulation.

The 3dMDface device consists of six cameras (see Figure 3.3) and four flash units. Two infrared cameras, one speckle flash unit, one texture flash unit, and one color camera are mounted on each side of the device. By projecting unstructured light patterns (see Figure 3.3.a) on the subject, the infrared cameras capture the geometry of the face, and a triangulation algorithm uses the light projection information combined with natural patterns of the skin to build the geometric meshes of the face. The color information captured by the color cameras are then mapped on the surface after the mesh reconstruction using a re-projection algorithm.

Before using 3dMDface system, the six cameras has to be calibrated. This device has an automatic calibration routine to align the cameras. A calibration plate consisting of an upside down "T" symbol should be positioned in front of the cameras, and after an automatic detection of the symbol, the 3dMD system tries to align the cameras automatically. This routine only takes 2 to 4 minutes.

As noted in [1], the acquisition time is about 1.5ms at the highest resolution, and the coverage is 180 degrees. The accuracy of the reconstructed geometry is reported as less than 0.2mm, however it is said to be $<$0.5mm by [32], and $<$0.6mm by [22].

3.5 Conclusion

In this chapter, we introduced different systems, such as laser scanners and photogrammetry, used for surface acquisition and explained their accuracies and capabilities. We then discussed why photogrammetry has become the preferred facial surface acquisition modality. We presented two challenges in photogrammetry, the correspondence problem and stereo-triangulation, and explained the mechanism of 3dMDface system used in this study.

In the next chapter, the necessity to fuse multiple modalities such as CBCT and photogrammetry is discussed, and the technique of registration is presented as a way to quantitatively measure the differences between imaging modalities.

Chapter 4

Multi-Modal Image Registration

4.1 Problem Definition

Image registration is the process of spatially aligning two or more images taken from the same patient, either at different times, or by different sensors.

Images taken from the same patient at different times are being registered to find, visualize, and evaluate the changes that happened in a specific time period. This registration method is referred to as multi-temporal single-modality image registration, and can be utilized in many clinical evaluations, such as monitoring teeth growth, and tracking orthodontic treatments.

Registering two or more imaging sensors, and extracting medical information from them may improve the accuracy of patient assessments. Processing different modalities includes properly registering them, hence making differences detectable. This procedure is referred to as multi-modal image registration. The application of this type of registration is necessary due to the advancements in imaging devices and techniques, and also due to the fact that no one modality can give a complete description of the patient conditions. Figure 4.1 shows an example of a multi-modal registration of skull and facial-skin, using CT and photogrammetry sensors from two different viewpoints.

As discussed in [33], CBCT technology has enabled capturing all possible maxillofacial radiographs in less than one minute with dosages that are much smaller than normal medical CT. Assessments of mandibular anatomy and position, and evaluation of anatomical surgeries can be accomplished by registering CBCT data.

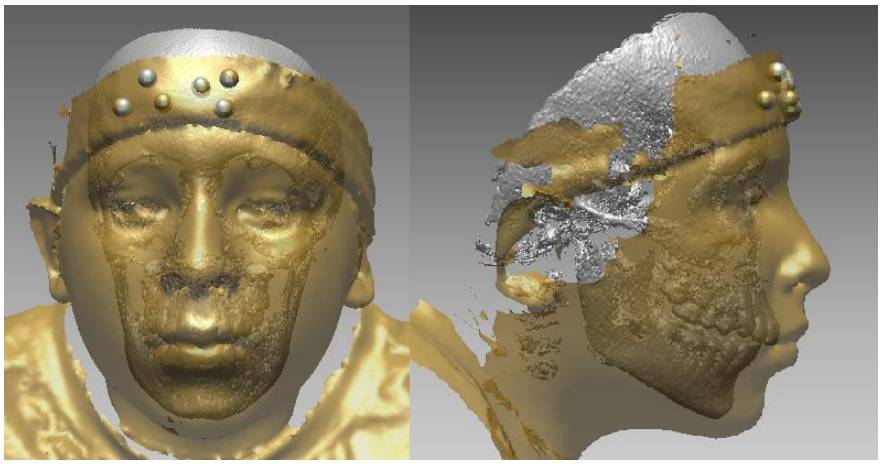

Figure 4.1: Multi-modal registration of skull and skin, using CT and photogrammetry sensors, from two different view points.

Cevidanes et al. [11] evaluated the registration of 3D models from CBCT data of 10 patients obtained before and after orthodontic surgery. Instead of using landmarks, they used the grey value information of the cranial base to register before and after-surgery images. The reproducibility of their method was confirmed under the hypothesis that the lower jaw should remain unchanged after the surgery.

However, since CBCT scanners cannot capture the true color texture of the skin, one should map the texture information onto the skull-based model. There have been some attempts to map the skin texture onto the conventional CT images. Khambay et al. [35] demonstrated that superimposition of 3D images of skull and skin extracted from 3D CT on to the 3D stereo photogrammetric images is possible. They introduced a methodology and performed this re-projection, and claimed an accuracy of their landmark-based registration method between 1.25 to 1.5mm.

One of the most important issues in dentistry today is the ability to track patients during and after treatments. Considering time as the fourth dimension gives us the ability to analyze the evolution of various structures during a specific time period. This method can either be done in real time, e.g. in studying chewing, or can be done over hours, days or even years as a treatment follow-up. Advances in medical imaging have led to creation of faster and better algorithms for reconstruction and analysis of 3D images over time.

Multi-modal registration of CBCT with stereo-photogrammetric data over time

gives us the ability to evaluate dental treatments more precisely and objectively. Boulanger et al. [9] have introduced a registration methodology for tracking based on a robust rigid registration algorithm. However, they have not reported the intrinsic landmarks used for long-term visit registrations, and do not describe the registration procedure for mandibles.

Due to the importance of evaluating orthodontic treatments and tracking mandible variations, we are introducing new methodologies for multi-modal and multi-temporal registrations of data obtained from CBCT and stereo-photogrammetry.

4.2 Registration Algorithms

4.2.1 Landmark-based Registration

Registering imaging modalities can be done using either extrinsic or intrinsic landmark-based methods [43]. "Landmarks" are points situated on meaningful parts of the subject, and represent the whole image for registration. Extrinsic registration methods are based on external objects attached to the subject. These objects should be clearly visible by all modalities, and should be easily detectable, either manually or automatically. Landmark-based registration method relies on the artificial landmarks to find the optimal geometric transformation between modalities.

Intrinsic registration methods are based on the intrinsic landmarks available on the patient without using any artificial object. A common way of performing intrinsic registration is to use anatomical landmarks that are unambiguous, visible parts of the anatomy of a patient, or user-defined geometrical points that are easily identifiable in different modalities.

The definition of landmark-based registration is as follows: For two sets of landmarks L_1 and L_2, each containing n points, find the best mapping that, for each point, minimizes the distance between the point in L_1 and the corresponding point in L_2. In other words, after the landmarks are determined on all images, each set of features should be mapped with the corresponding ones in the other image. In this sense, a transformation matrix, corresponding to a rotation and translation, can be determined to match the rest of the points, while minimizing the distance.

Given two sets of landmark points $\mathbf{L}_1$ and $\mathbf{L}_2$, a rotation matrix R, and translation vector $\mathbf{T}$, the following formula provides the transformation matrix M:

$$M(L_i) = \mathbf{L}_j = R\mathbf{L}_i + \mathbf{T}\cdot$$

Now that the mapping function is determined, it should be optimized to minimize the distance between the corresponding points. A common function of measuring this distance is the Sum of the Squared Distances (SSD), which is defined as follows:

$$D(M, L_1, L_2) = \sum_{i=1}^{n} ||M(l_{1_n}) - l_{2_n}||^2\cdot$$

Hence, the definition of registration would be as below.

For sets of landmarks L_1 and L_2, with n corresponding points,
Find rotation matrix (R) and translation vector (T) such that:

The following distance function is minimized.
$D(M, L_1, L_2) = \sum_{i=1}^{n} ||M(l_{1_n}) - l_{2_n}||^2 = \sum_{i=1}^{n} ||Rl_{1_n} + T - l_{2_n}||^2$

4.2.2 Iterative Closest Point (ICP)

The most commonly used registration method for landmark-based registrations was proposed by Besl et al. [8] in 1992, and is known as "Iterative Closest Point (ICP)". As discussed in [43], its versatility, speed, and ease of implementation made it a very popular registration method.

According to Ezra et al. [17], the definition of ICP algorithm is as follows: For two shapes of S_1 and S_2, find the best mapping for S_1, i.e. closest points C_{S_2}, that uses translation and rotation to match S_2 as well as possible.

Various cost functions have been used in different ICP implementations to find the best transformation from S_1 to S_2, two of which are defined below:

1. Hausdorff Distance

   $F(S_1, S_2) = max_{s \in S_1} ||s - C_{S_2}(s)||$

2. Sum of the Squared Distances

   $F(S_1, S_2) = \frac{1}{m} \sum_{s \in S_1} ||s + t - C_{S_2}(s + t)||^2$

The ICP algorithm uses the Sum of the Squared Distances to minimize $F(S_1 + t, S_2)$ over all the possible transformations t consisting of translations and rotations. It starts with an initial estimate of the transformation, and iteratively tries to align S_1 on S_2, while decreasing the cost function F. This method is guaranteed to converge to a local minimum [14].

As explained in [17], considering $t_0 = 0$, at each iteration i, the shape S_1 has been transformed by t_{i-1}. Then each translated point $s + t_{i-1} \in S_1 + t$ is assigned to its closest point $C_{S_2}(s + t_{i-1})$. Once the set of closest points are found, the new transformation Δt that minimizes the cost function F is computed. More specifically, the cost function minimized is the following:

1. Hausdorff Distance

   $F(S_1 + t_{i-1}, S_2) = max_{s \in S_1} ||s + t_{i-1} + \Delta t_i - C_{S_2}(s + t_{i-1})||$

2. Sum of the Squared Distances

   $F(S_1 + t_{i-1}, S_2) = \frac{1}{m} \sum_{s \in S_1} ||s + t_{i-1} + \Delta t_i - C_{S_2}(s + t_{i-1})||^2,$

and the new transformation would be $t_{i-1} + \Delta t_i$. The algorithm terminates if the cost function is below a pre-defined threshold. The following is a step-by-step procedure for ICP algorithm.

```
Input:  Initial estimation of the transformation
For ∀s ∈ S1:
  1.  Assign s + t_{i-1} to its closest point in S2  (C_{S2}(s + t_{i-1}))
  2.  Find Δt such that the following cost function is minimized:
      F(S1 + t_{i-1}, S2) = (1/m) Σ_{s∈S1} ||s + t_{i-1} + Δt_i − C_{S2}(s + t_{i-1})||^2,
  3.  Terminate if the error is below a defined threshold.
```

Figure 4.2.a shows the initial estimation of the transformation obtained via an extrinsic landmark-based method, and Figure 4.2.b represents the final transformation after the ICP algorithm is applied on the data.

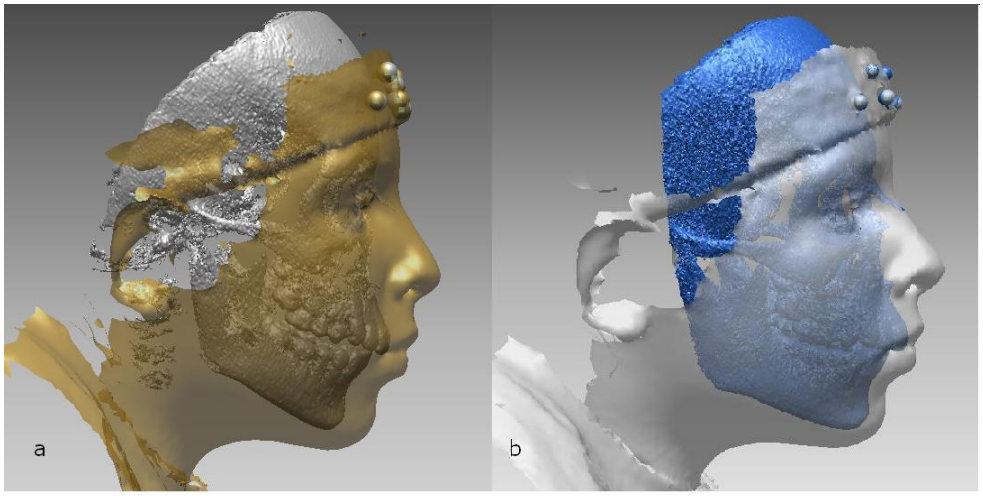

Figure 4.2: a: The initial estimation of the transformation, and b: The final transformation after the ICP algorithm is applied on the data.

One of the key elements of the ICP algorithm is its ability to determine rapidly the closest points. The brute force implementation is $N \times M$ where N is the number of points in the first set, and M is the number of points in the second set. This could make the ICP very slow for large datasets. A better point search algorithm can be found such as the k-D tree explained in [55] where a binary search tree for k-dimensional data is used to partition the space, and find the closest points. Using this algorithm, the search complexity can be reduced to $N \log M$.

Other improvements of the ICP algorithm include:

- Using robust statistics, which make the ICP robust to outliers [12],
- Stochastic search for global minimum based on very fast simulated annealing [41], and
- Implementation of ICP algorithm for Graphics Processing Unit (GPU) [36].

4.3 Natural Landmarks for Multimodal Image Registration

The fundamental step for landmark-based registration is the selection of landmarks, and positioning them where it helps obtaining more accurate registration results. In case of attaching extrinsic landmarks to the subjects, landmarks should be made

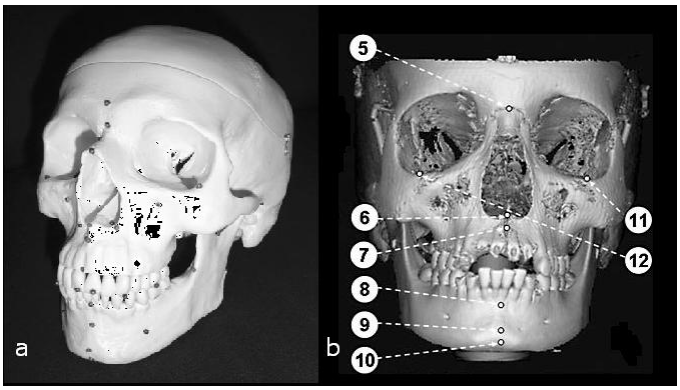

Figure 4.3: a: 28 landmarks placed on the skull. From Stratemenn et al. [57]. b: 10 landmarks out of 14 utilized for skull measurements. From Periago et al. [50].

from a material that does not interfere with the imaging source. For example in CT imaging modality, the landmarks should be made of a material that does not scatter X-ray. They should also be visible and traceable through all the modalities involved in the registration procedure.

Utilizing implantable markers as extrinsic landmarks gives surgeons and radiologists the opportunity of having highly accurate registration results. They can be precisely identified in CT, and their position does not change during the imaging process [19]. However, this method is considered highly invasive, and the need for non-invasive procedures has focussed many researchers on anatomical landmarks belonging to the bone surface instead.

In contrast to extrinsic landmarks, the positioning of natural landmarks on the human body is much more difficult. These landmarks should be easily detectable in all the modalities, and should not change position or grow in case of multi-temporal image registration.

Many studies on natural landmarks can be found in the literature [57, 50, 27, 19] and have been devoted to finding the validity of skull measurements. In the following section, we will discuss four studies that took advantage of skull landmarks and how they can be used to register modalities.

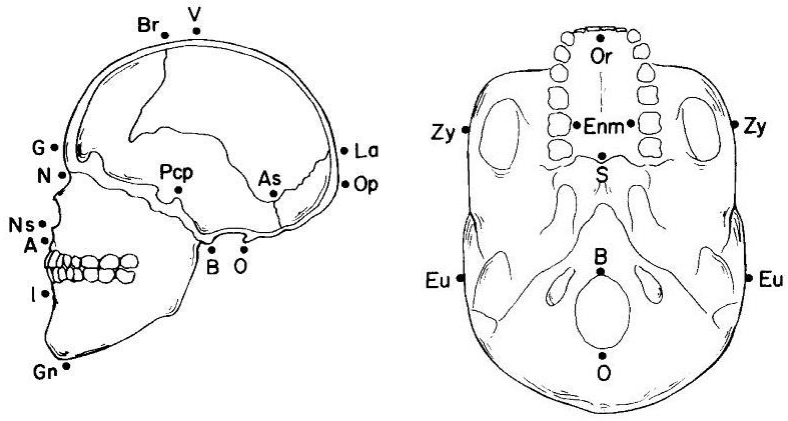

Figure 4.4: Landmarks used for investigating the accuracy of skull measurements. From Stratemenn et al. [27].

4.3.1 Skull Landmarks

Stratemann et al. [57] tried to determine the accuracy of linear measurements between orthodontic landmarks located on the skull. They compared the measurements taken from two CBCT systems with real measurements made with a calliper. The authors used 28 external spherical landmarks to make 125 linear measurements. Figure 4.3.a depicts all the landmarks placed on the skull model. The registration has been done by picking the center of the spheres, which helps minimize landmark identification error. This method is used in our study as well.

Periago et al. [50] conducted similar research with the use of fourteen anatomical landmarks, ten of which are depicted in Figure 4.3.b. They showed that most craniofacial linear measurements made from CBCT are sufficiently accurate for craniofacial analysis. Hildebolt et al. [27] made 29 standard measurements on two normal and three deformed skulls. They found the difference between the reference calliper measurements and those made from images. The craniofacial landmarks were selected from standard craniofacial ones introduced in [29]. Figure 4.4 shows the landmarks located on the skull. This study showed that equivalent measurements can be made in comparison to calliper references.

Fieten et al. [19] introduced a new method for registration of cranial CT images. They used skull landmarks depicted in Figure 4.5.a to compare their own results with the registrations produced by the ICP algorithm.

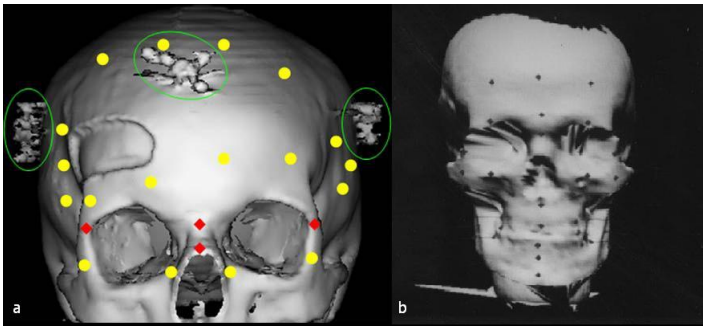

Figure 4.5: a: Skull landmarks. Red anatomical landmarks used for pre-registration. Yellow surface points used for surface-based registration. Green ellipses are bone-mounted markers. From Fieten et al. [19]. b: Landmarks on digitized skull. Couresy of Vanezis et al. [60].

In addition, many studies on the accuracy of skull measurements have been conducted to construct 3D models of the face and the skull. Vanezi et al. [60] took advantage of skull landmarks to fit a 3D facial image over a skull image, to reconstruct a human face. The skull landmarks used in that study are shown in Figure 4.5.b. They introduced other applications of 3D reconstruction in identification of murder victims, and reconstruction of archaeological skulls.

4.3.2 Mandible Landmarks

There are a number of studies in the literature that use mandible landmarks. Nielsen et al. [10] developed a physically valid model for registration of time sequence images of the mandible. They collected three images of one person's mandible at different times, and registered them with the use of a physical bone growth model. They used the fact that bones grow from their surface, not from their interior. As a result, they suggested the inferior dental nerve channel, the inner cortical surface of symphysis, and the tip of the chin, as stable features of the mandible, suitable for jaw registration. One can see the location of those landmarks in Figure 4.6.

Afsar et al. [2] have used the mandible features shown in Figure 4.7.a. to assess the precision of panoramic radiographs. They showed that the panoramic radiographs are as good as oblique cephalonetric radiographs. In another study, Williams et al. [62] investigated the accuracy of the human mandible landmarks, and introduced a set of mandibular landmarks that can be used for evaluating craniofacial

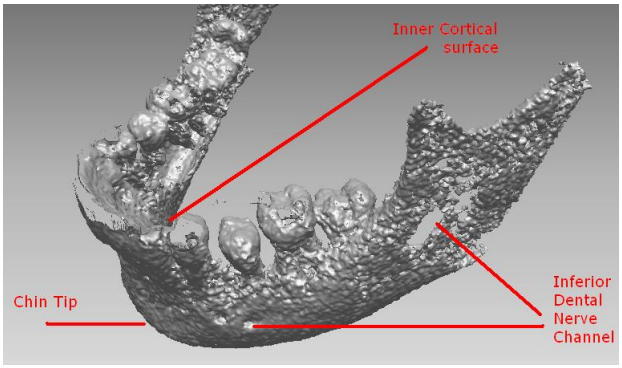

Figure 4.6: Three mandible landmarks which are suggested for registration use.

disorders and biological processes. The suggested landmarks are depicted in Figure 4.7.

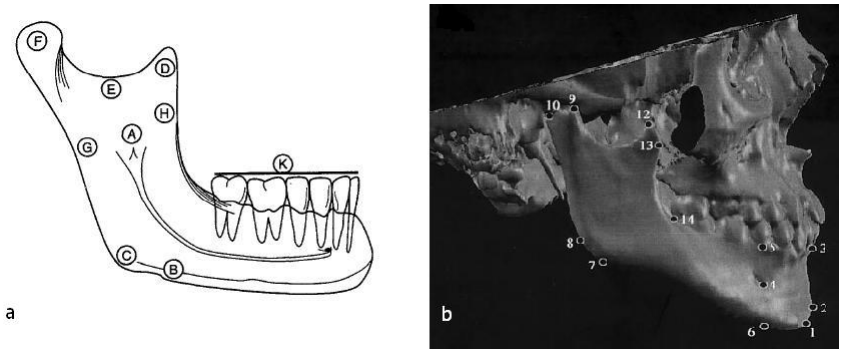

Figure 4.7: Anatomical landmarks for mandible. a: landmarks used for assessments of panoramic radiographs (from Afsar et al. [2]). b: Possible mandible landmarks which can be used for mandible research (from Williams et al. [62]).

4.4 Selected Anatomical Landmarks for our Study

Figure 4.8 shows a set of 13 possible anatomical landmarks of skull, based on the literature reviews presented in Section 4.3.1. Since the mandible moves independently to the upper-skull, it should be segmented and analyzed separately. Therefore, feature points 11, 12, and 13 cannot be used as skull anatomical points in our study. Moreover, feature points 9 and 10 are situated down the nose and up the teeth. These points cannot be considered as suitable landmarks since the bony structures of those parts can grow in an 8-12 months period during which our data has been acquired, and therefore cannot be identified as stable landmarks for our

study. Feature points 2, 5, and 7 are located in areas which can be affected by the segmentation algorithms. These areas might result in different structures when segmented from the CBCT data, and therefore may not be easily identifiable in all the images of different times. The remaining points which are points 1, 3, 4, 6 and 8 can be considered as stable anatomical landmarks for skull, since they are all easily identifiable through images of both times, and they do not change position or grow during the acquisition period.

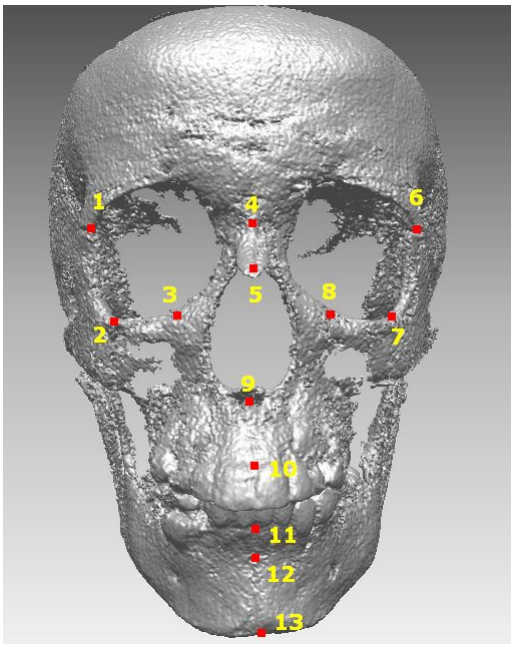

Figure 4.8: Possible anatomical landmarks for skull, based on natural feature points used in the literature.

Different anatomical landmarks have also been studied in the literature that was reviewed in Section 4.3.2. Nielsen et al. suggested the three feature areas shown in Figure 4.6 for the mandible registrations due to their stability. Among these areas, the tip of the chin is not considered a possible landmark in our study, since the skull segmentation process might affect the exact place of it. However, the inner cortical surface and the inferior dental nerve channels illustrated in Figure 4.9 were selected for the mandible registration in this study.

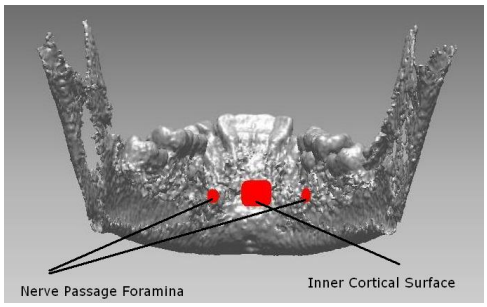

Figure 4.9: Possible anatomical landmarks for mandible, based on natural feature points used in the literature.

4.5 Conclusion

In this chapter, we addressed the problem of tracking orthodontic patients over time, and we explained multi-modal registration as a solution to our problem. Then two registration methods of landmark-based, and template-based iterative closest point algorithms were presented. Then different skull and mandible landmark systems used in the literature for registration were introduced, and a selection of stable and identifiable landmarks for our study was also presented.

In the next chapter, we will represent our registration procedure for solving the problem of tracking patients over time, and we will evaluate the methodology with different validation techniques.

Chapter 5

Experimental Results

As discussed in Section 4.1, combining CBCT for 3D bone shape measurement, with 3dMD for face-skin shape measurement is necessary for the complete tracking of shape variations of orthodontic patients. Soft tissues as well as teeth and jaw displacements can be viewed, measured and evaluated between visits occurring at $Time_1$ (T_1) and $Time_2$ (T_2).

In this chapter, we explain a methodology to track face-skin and bony structures of the human head, after a maxillofacial treatment has been performed. We introduce three registration methods,

1. Phase 1:

    - Extrinsic landmark-based registration of multi-modal CBCT and 3dMD data at each visit;

2. Phase 2:

    - Intrinsic landmark-based registration of single-modal multi-temporal CBCT data of the skull, between two visits at T_1 and T_2;
    - Intrinsic landmark-based registration of single-modal multi-temporal CBCT data of the mandible, between two visits at T_1 and T_2.

5.1 Data Acquisition

As shown in Figure 1.1, the proposed tracking procedure consists of four steps. In the first step, six subjects were chosen from an ongoing clinical trial. Three of these data sets were from untreated controls (Subjects 2, 3 and 5), and the other three (subjects 1, 4 and 6) were from treated patients undergoing a treatment. Six Titanium spheres with a diameter of 6.5mm were located on a head-band, which was placed on patient's forehead during each imaging session.

For each subject, multi-modal images of CBCT and stereo-photogrammetry were acquired at each visit at times T_1 and T_2 within an 8-12 month period. A NewTom QR-DVT9000 CBCT scanner described in Section 2.5 was used to measure the bone structure, and a 3dMDface system described in Section 3.4 was used to capture the patient's head skin. Ethical approval was granted by the University of Alberta Health Research Ethics Board, HREB during the test period.

5.2 Pre-processing Procedure

The pre-processing procedure includes applying different filters and algorithms to the CBCT and 3dMD data separately, in preparation to the experimental analysis.

For CBCT, the raw data saved in DICOM (Digital Imaging and Communications in Medicine) format were converted to a VTI format, which could be viewed and edited by an open-source volumetric data processing and visualization software called Paraview. This conversion process was done by the Volview software. The resolution of the volumetric CBCT data was 512 x 512, with 256 grey levels per pixel.

A Marching Cubes filter was used in Paraview to extract the skull geometry from the CBCT density values. An iso-density value of 950 was used to separate bone tissues from the rest. One can see in Figure 5.1.b the surface data produced by the Marching Cubes algorithm. After extracting the skull geometry, a decimating filter was applied to reduce the number of triangles produced from the Marching Cubes algorithm. One can see in Figure 5.1.b that the decimated geometry (at 80%) does not produce any noticeable differences. This decimation is essential, as large

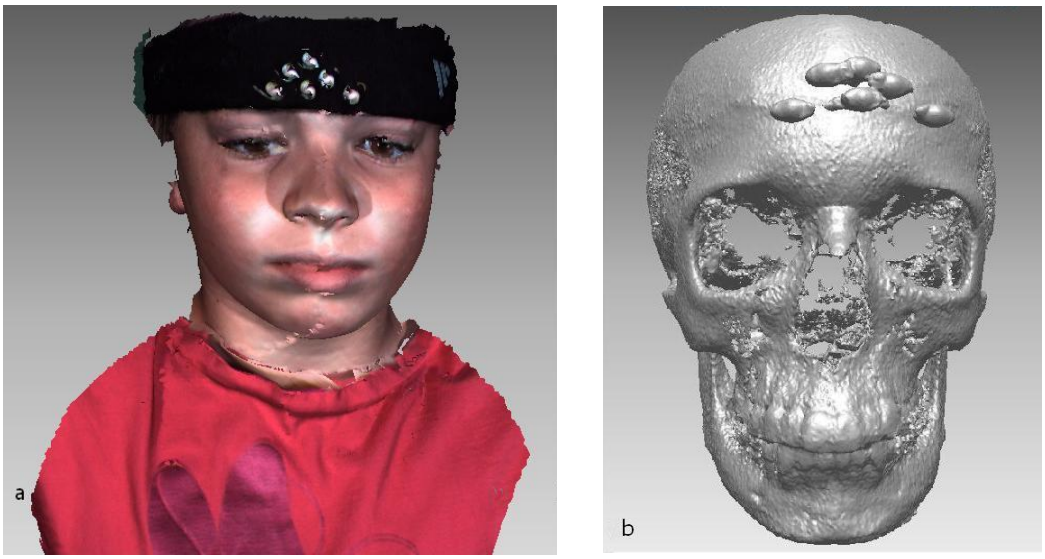

Figure 5.1: 3D surface representing different density values regarding (a) skin and (b) skull.

polygon counts are hard to process and cannot be displayed easily in real-time.

For the 3dMD data, the calibrated system digitized the patient after being scanned by the CBCT. After the four infrared and the two high-resolution color images (see Figure 3.3.a) were acquired and transferred to the processing workstation, the software extracted a geometric mesh (see Figure 5.1.a) by solving the correspondence problem from the four infrared images. Using the calibration parameters, the corresponding points measured in 3D and the extracted measurements were triangulated and back-projected onto the high-resolution color images. The result was a textured polygonal data with approximately 50K triangles. The polygonal data was saved into an OBJ format and loaded into the Rapidform software to be further processed. The textured polygons were converted from vertex to texture definition to vertex to color, which allowed to move the color information at the same time as the vertices during registration.

One can see in Figure 5.1.a the polygonal face information from 3dMD, and in Figure 5.1.b the corresponding skull polygons from the CBCT data at time T_1 for $patient_1$.

5.3 Methodology

A complete tracking of the shape variations for the head skin and bone structures necessitates a multi-modal and multi-temporal registration of CBCT and 3dMD data, which are obtained at different times.

The registration procedure, illustrated in Figure 1.1 can be divided into two phases. The first phase consists of performing the multi-modal registration of the CBCT and the stereo-photogrammetry data at each visit. The second phase uses the results of the first phase saved as a polygonal shell grouping the registered polygons from the head skin and the skull into a common coordinate system. The two shells at T_1 and T_2 are then registered together using intrinsic landmarks on the skull and applied to each shell. The following sections describe the registration procedure.

5.3.1 Phase 1: Multi-Modal Registration of CBCT and 3dMD

The first phase includes multi-modal registration of CBCT and 3dMD data at each visit. For this procedure, we utilized the extrinsic, landmark-based registration method.

To accomplish extrinsic landmark-based registration, it is necessary to have extrinsic landmarks that do not scatter the radiation beam and are clearly identifiable in both modalities. As described in Majid et al. [44], five to eight pairs of landmarks are necessary to obtain high accuracy registration results. Therefore six Titanium spheres with a diameter of 6.5mm were glued on a head-band. The headband was placed on patient's forehead during the entire imaging procedure.

Rapidform, a commercial polygon processing software was used to register the polygons from the CBCT and 3dMD. To register those geometries, we started by first registering the extrinsic landmarks pairwise. In order to do so, we had to first fit spheres on the polygons corresponding to the sphere. We first selected the polygons in both data sets and then used a mean square sphere fitting routine with a fixed radius of 3.25mm. From the fitted spheres, the estimated centers were used as the reference points for data sets to be registered. Figure 5.2 shows the virtual spheres fitted on the headbands' spheres, for both the 3dMD and the CBCT data sets.

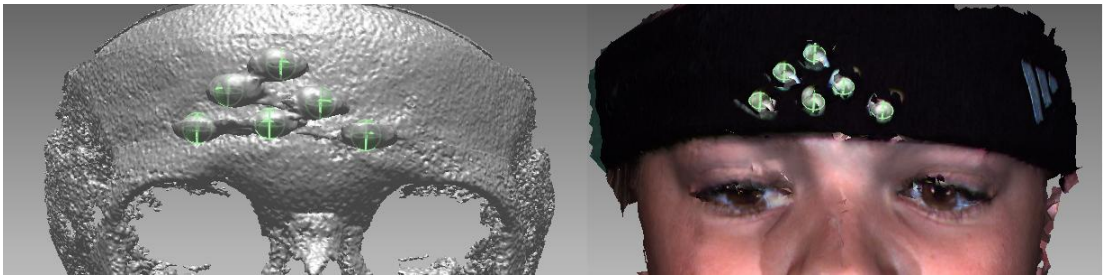

Figure 5.2: Green virtual spheres fitted on the headband. These fitted spheres are then used as extrinsic landmarks for the registration of 3dMD and CBCT data.

After finding each reference sphere's center, a transformation matrix was found between the corresponding points using a point registration routine provided by the Rapidform. The same transformation was applied to the CBCT geometry to bring it in registration with the 3dMD data. This registration process was explained in Section 4.2.1. The coarse registration result was then used as a starting point for an ICP algorithm which is used to provide a more accurate registration result. The results for all six registered spheres are shown in Figure 5.3 and in Figure 5.4. As illustrated, the blue and the silver target points are perfectly aligned, and the skull and the skin shells are registered while keeping a reasonable distance in between. The registration results with and without applying ICP algorithm are also illustrated. Figures 5.5 and Figure 5.6 show the effect of ICP algorithm on T_1 data, and Figures 5.7 and Figure 5.8 present the T_2 results. As depicted, the distances between the skull and the skin are changed after applying ICP, which improved the registrations.

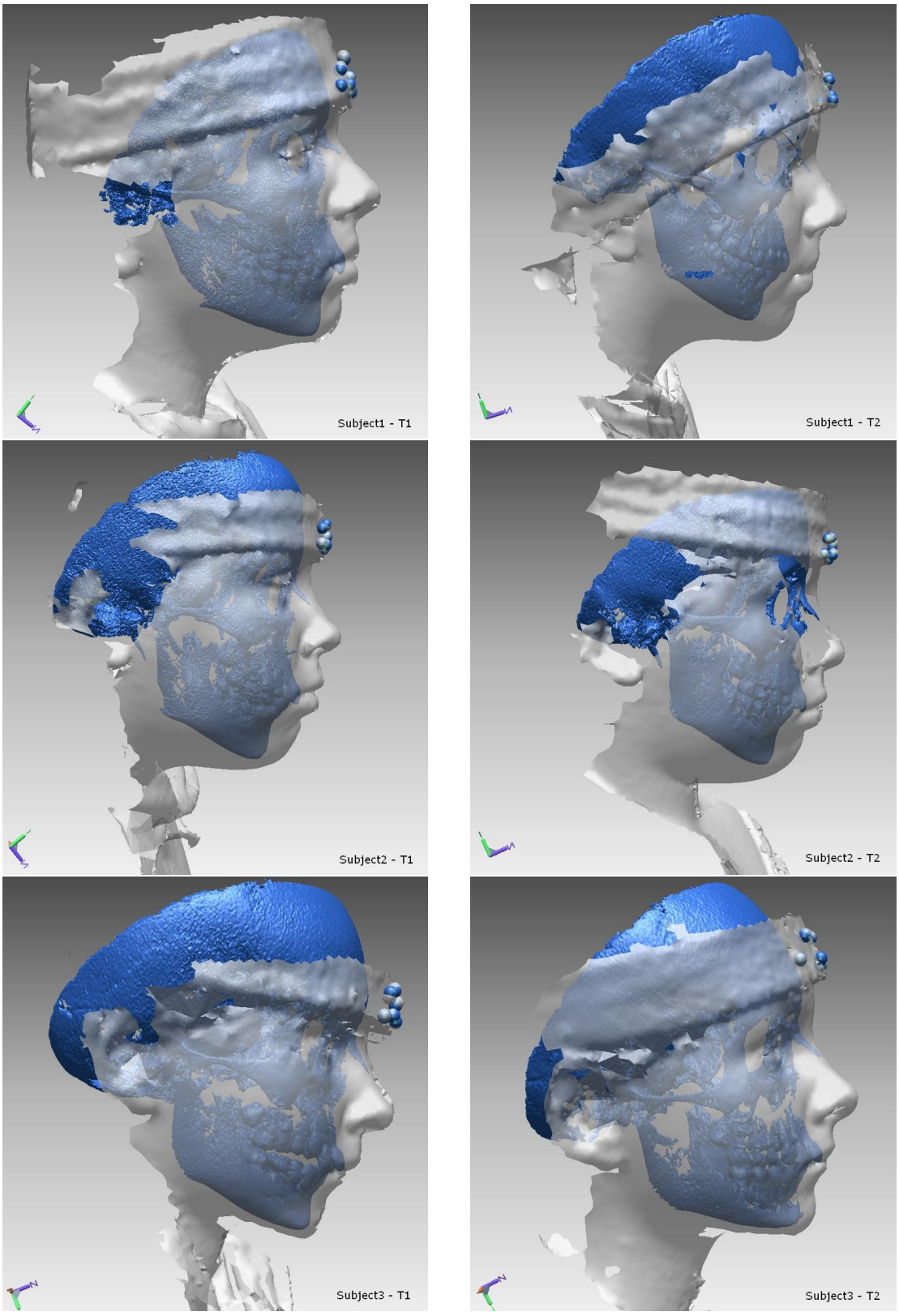

Figure 5.3: Registration results of multi-modal data of CBCT and 3dMD for Subjects 1-3, for T_1 (left), and T_2 (right). As shown, the blue and the silver target points are perfectly aligned, and the skull and the skin shells are registered while keeping a reasonable distance in between.

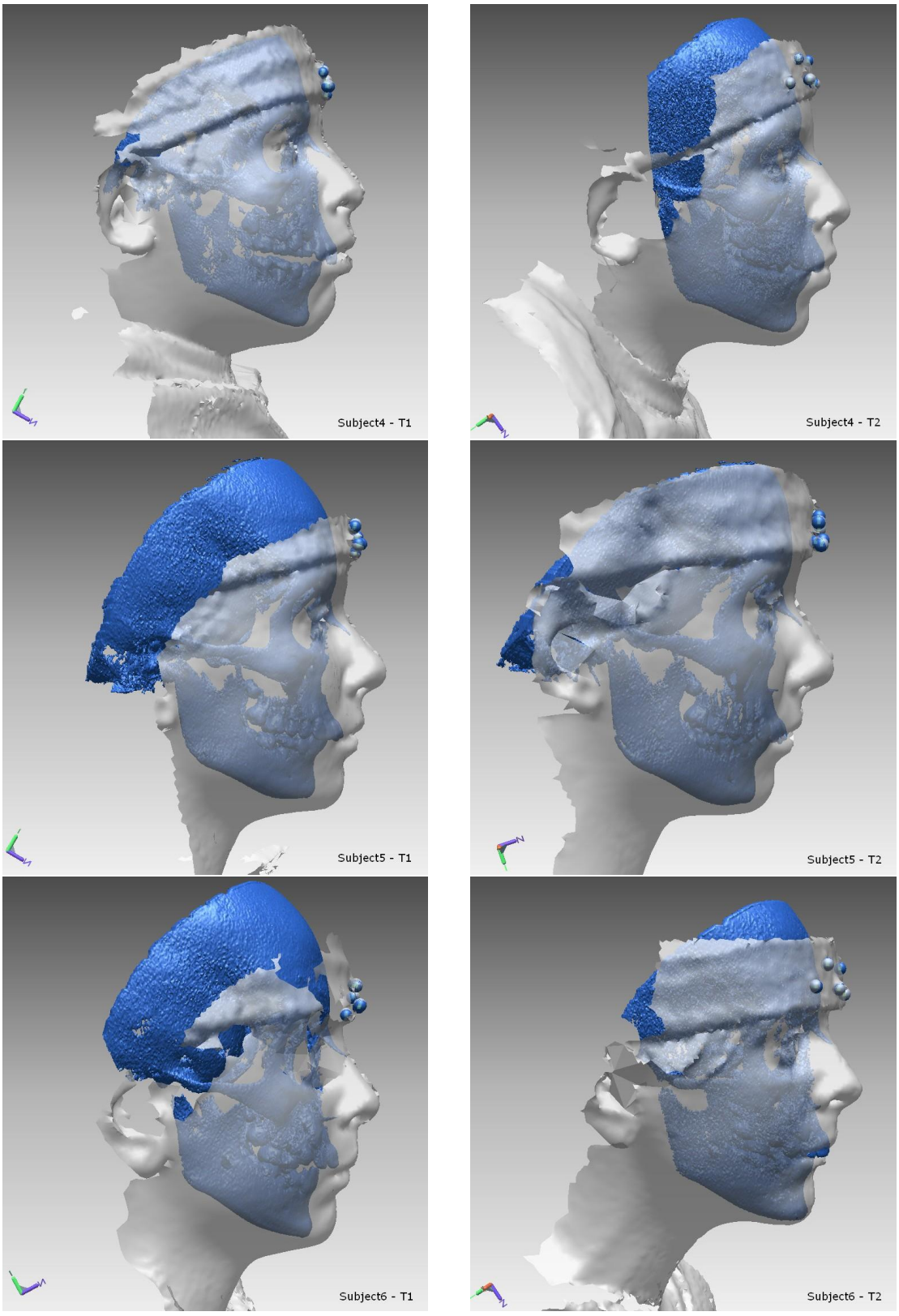

Figure 5.4: Registration results of multi-modal data of CBCT and 3dMD for Subjects 4-6, for T_1 (left), and T_2 (right). As shown, the blue and the silver target points are perfectly aligned, and the skull and the skin shells are registered while keeping a reasonable distance in between.

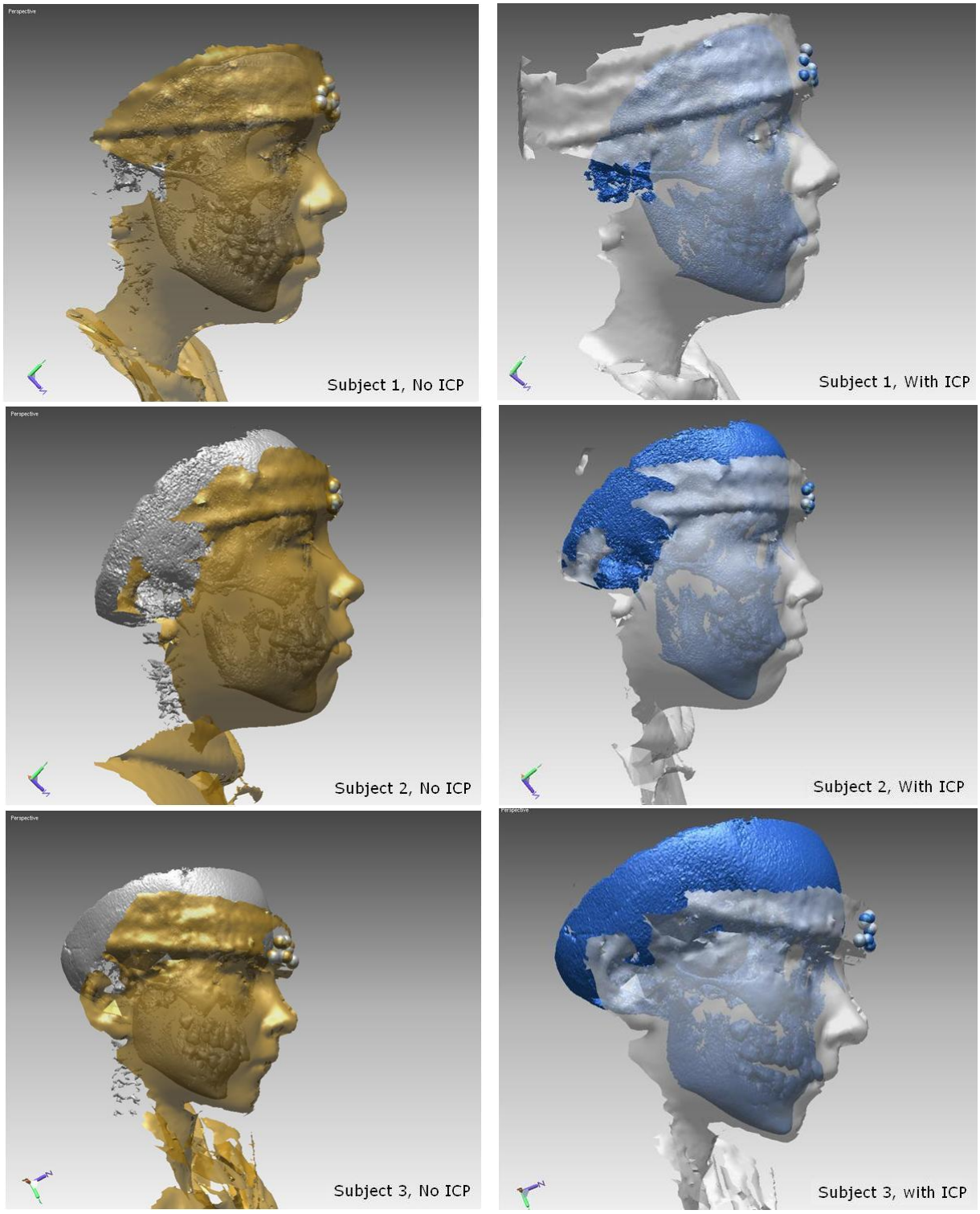

Figure 5.5: Registration results of multi-modal data of CBCT and 3dMD for T_1 images, obtained from $Subject_1$ to $Subject_3$. The left pictures show the result of landmark-based registration algorithm and the right pictures show the effect of the ICP algorithm on them. As depicted, the distances between the skull and the skin are changed after applying ICP, which improved the registrations.

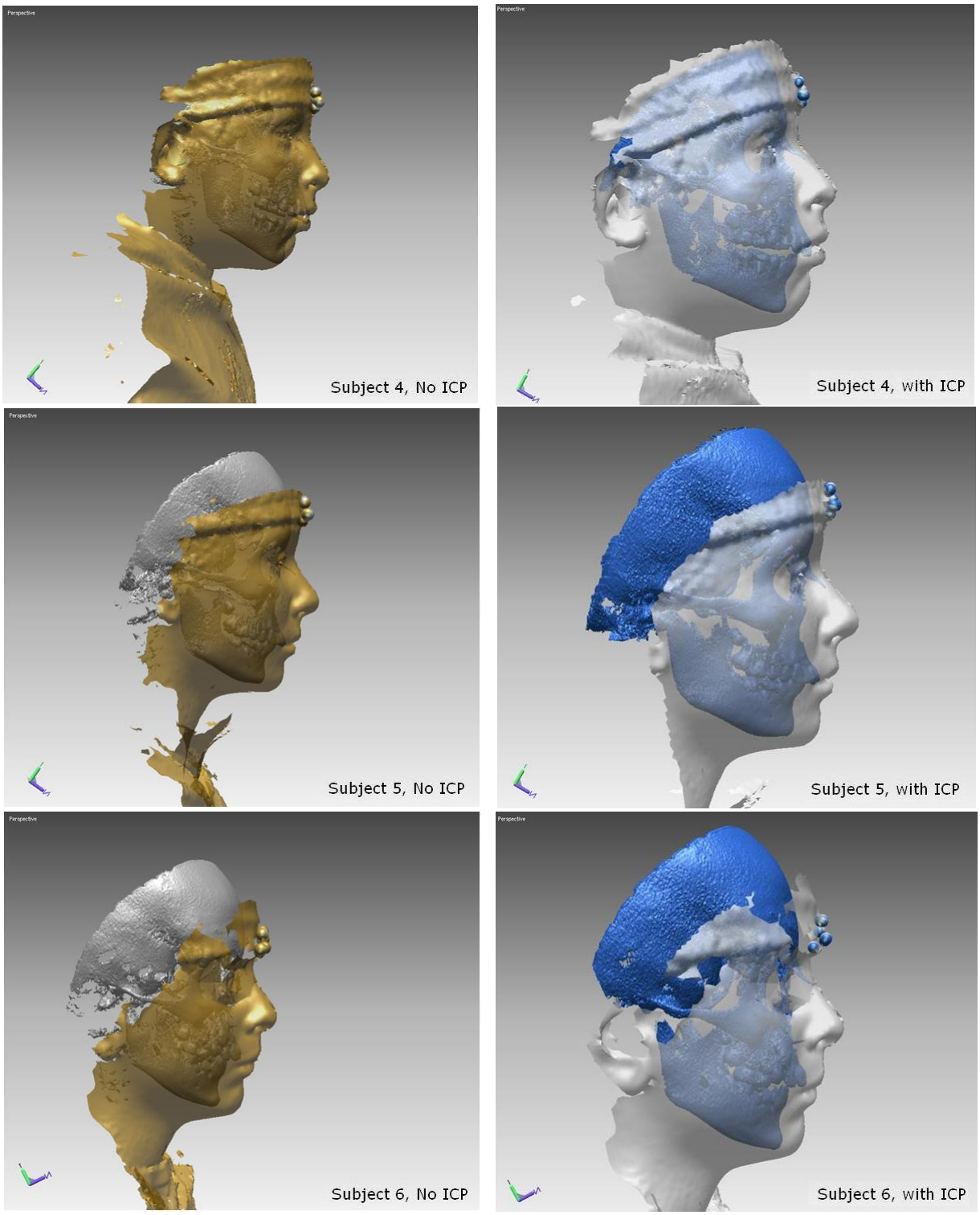

Figure 5.6: Registration results of multi-modal data of CBCT and 3dMD for T_1 images, obtained from $Subject_4$ to $Subject_6$. The left pictures show the result of landmark-based registration algorithm, and the right pictures show the effect of the ICP algorithm on them. As depicted, the distances between the skull and the skin are changed after applying ICP, which improved the registrations.

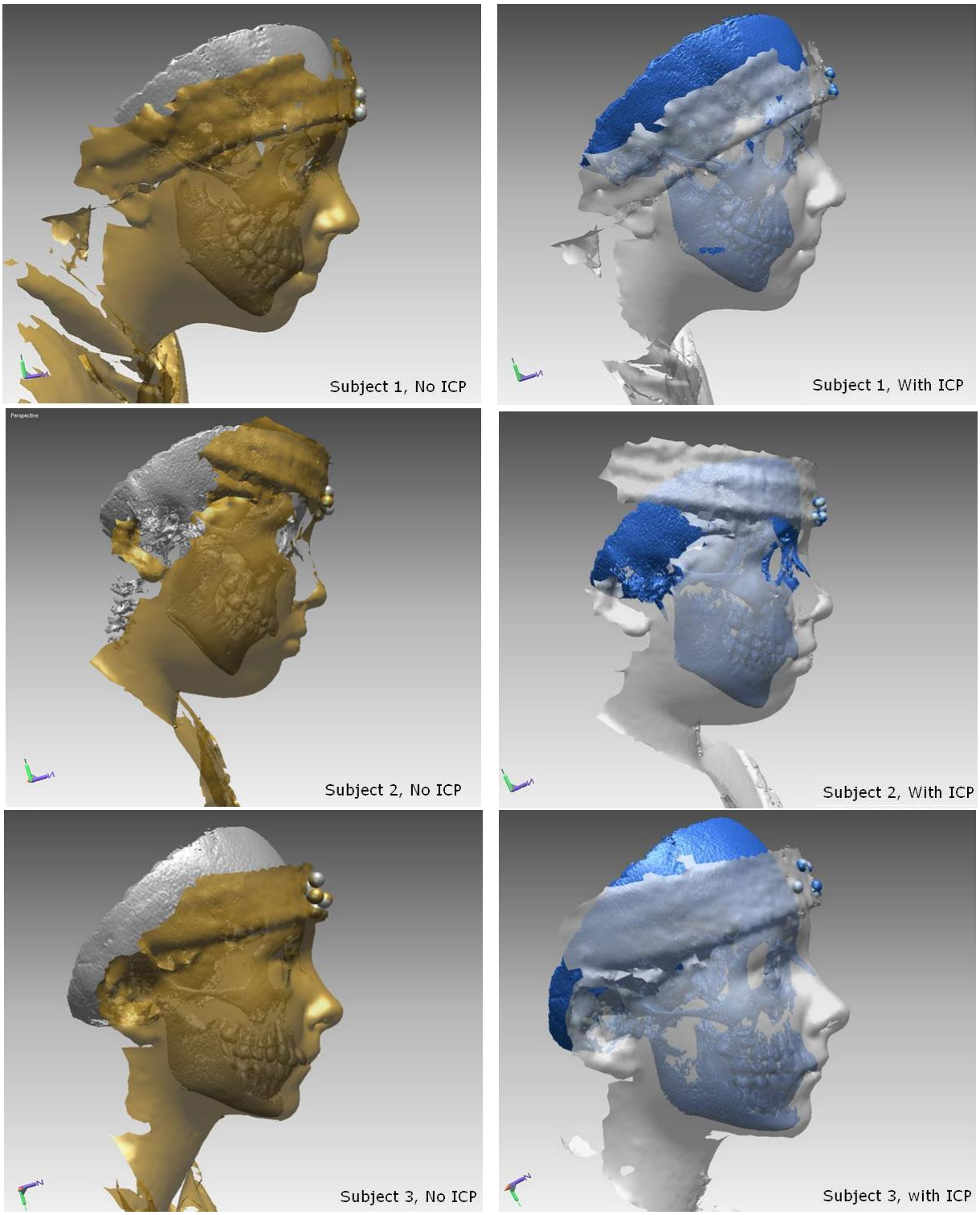

Figure 5.7: Registration results of multi-modal data of CBCT and 3dMD for T_2 images, obtained from $Subject_1$ to $Subject_3$. The left pictures show the result of landmark-based registration algorithm and the right pictures show the effect of the ICP algorithm on them. As depicted, the distances between the skull and the skin are changed after applying ICP, which improved the registrations.

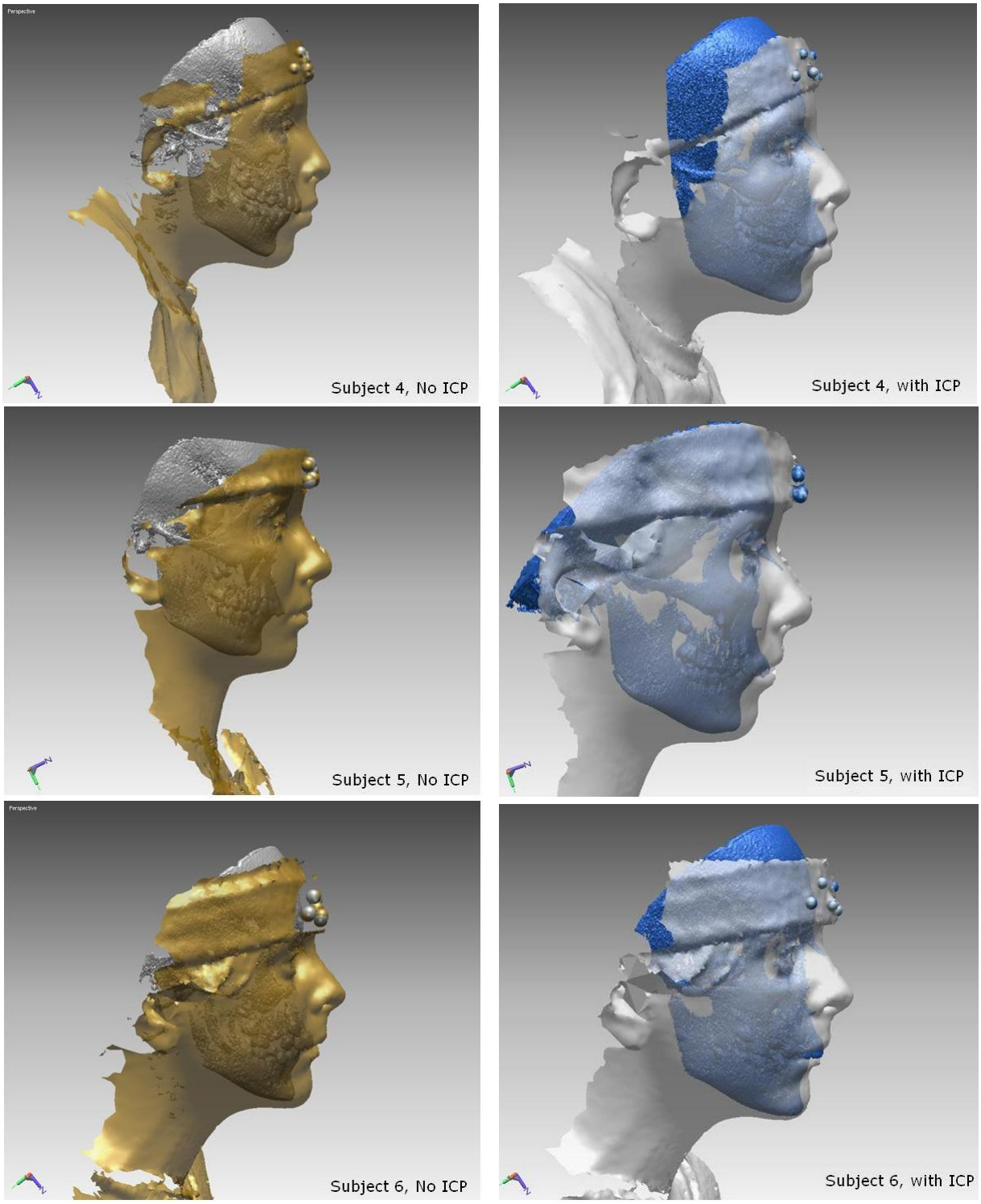

Figure 5.8: Registration results of multi-modal data of CBCT and 3dMD for T_2 images, obtained from $Subject_4$ to $Subject_6$. The left pictures show the result of landmark-based registration algorithm and the right pictures show the effect of the ICP algorithm on them. As depicted, the distances between the skull and the skin are changed after applying ICP, which improved the registrations.

5.3.2 Phase 2: Multi-Temporal Registration

Once the multi-modal data are registered for each visit at time T_1 and T_2 separately, a methodology for multi-temporal registration was developed. The result of this procedure is that the polygon set from T_1 is registered with the one at time T_2. The challenge of this process is that it is impossible to guarantee that the spheres are at the same location in different visits. Furthermore, the subjects' face shape and lower jaw may not be the same as it is under treatment. Therefore, we used intrinsic anatomical landmarks for multi-temporal registration.

Moreover, since the mandible moves independently from the upper skull, it should be analyzed separately. For each skull in T_1 and T_2, the mandibles are segmented manually from the upper skull using a polygon selection tool in Rapidform. As a result, the multi-temporal registration was done as a separate process for the mandible and the skull.

Multi-Temporal Registration of Skull

Since choosing intrinsic landmarks on 3dMD data were difficult due to its constructions around eyes and nose, we decided to use the skull data to deal with the in-between visit registration. In order to use the skull, intrinsic anatomical landmarks have been selected to be mapped and used for multi-temporal registration.

The anatomical landmarks chosen from the skull, which are discussed in Section 4.4, are shown in Figure 5.9. These landmarks are easily identifiable at both times and are stable over long periods. Once the points are selected on the CBCT data, intrinsic landmark-based registration method is applied, and the two skulls are registered. By applying the same transformation on the entire polygon shell, the 3dMD skin data, which had been registered with CBCT data in phase 1, is also registered. From the initial estimate of the landmark registration, an ICP algorithm is then used to optimize the quality of the registration. In this study, the maximum average for deviations are set at 1mm. This parameter is set to eliminate outliers, which due to [52] has a positive effect when ICP is performing least-square minimization.

To represent the registration results, the signed distances (in mm) for the corre-

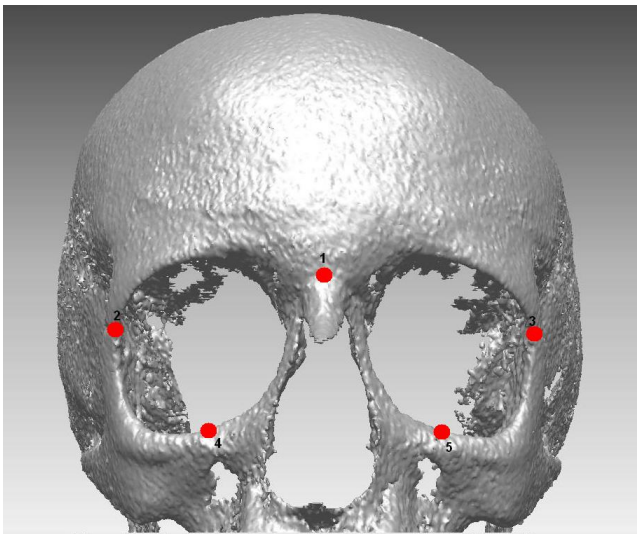

Figure 5.9: Anatomical skull landmarks used for multi-temporal registration of CBCT data, from T_1 to T_2.

sponding points between T_1 and T_2 shells were measured as the registration errors. Then for each patient, a diagram of error distribution was plotted, and the corresponding color-coded map of the error distribution was visualized on the patient's skull. As illustrated in Figure 5.11, the signed distances are the distances of datapoints from their closest triangles along with a positive or negative sign due to the position of the point relative to the triangle normal (inside or outside). The dark colors which show more extreme deviations are only present at the borders which is due to the segmentation, and on the front teeth which shows the growth of the teeth during the treatment. The rest of the skulls seem to have a distribution error around zero, which shows the effectiveness of the registration procedure. Moreover, Figures 5.12 and 5.13 also represent the effect of the ICP algorithm on the multi-temporal skull registration. The left columns show the results before, and the right columns show the results after the use of the ICP algorithm. As one can see in the diagrams of deviation distributions, the registration errors are distributed around zero after applying the ICP algorithm, which means that the distances between the corresponding points have been improved, and the precision of the registration results are optimized by this algorithm.

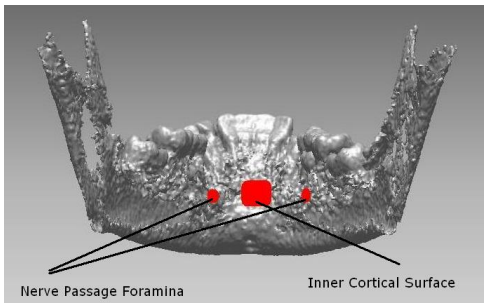

Figure 5.10: Anatomical mandible landmarks used for multi-temporal registration of CBCT data, from T_1 to T_2.

Multi-Temporal Registration of Mandible

Similar to the skull registration, one has to use intrinsic landmarks to register the mandibles between trials. Therefore, anatomical landmarks were chosen as discussed in Section 4.3.2. Nerve passage foramina and the inner cortical surface were selected, as shown in Figure 5.10. As in the skull registration, the landmark-based registration was first used to initialize an ICP optimization. The graph of error distribution as well as the corresponding color-coded map was visualized on each patient's mandible. As shown in Figure 5.14, the dark colors are only located at the borders due to the manual segmentation. The rest of the mandible registrations seem to have a distribution error around zero, which shows the effectiveness of the registration procedure. Moreover, One can see the effect of the ICP algorithm on the registration procedure in Figure 5.15 and Figure 5.16. The left columns show the results before, and the right columns show the results after the use of ICP algorithm. Again, the registration errors are more distributed around zero after applying the ICP algorithm, which means that the registration between the corresponding points have been improved, and the registration results are optimized by this algorithm.

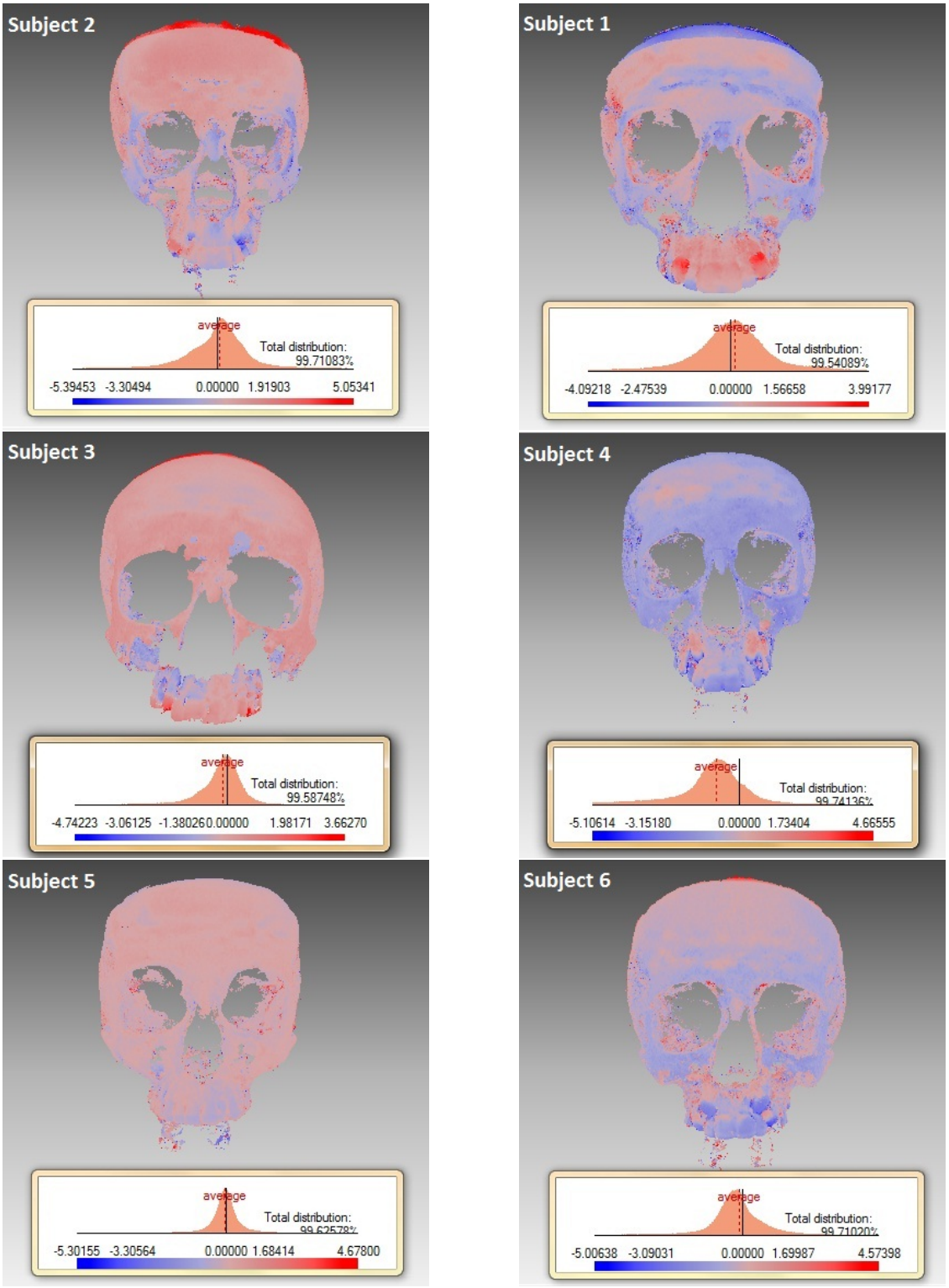

Figure 5.11: Results of registered skulls between $T1$ and $T2$ using intrinsic landmark-based method. The left column shows the results for untreated subjects and the right column represents the procedure for treated ones. The dark colors represent larger registration errors (in mm) on the skulls, and the graphs show the distribution of signed deviations for the registration errors. As shown, the errors are distributed around zero, meaning that the registration procedure is not biased.

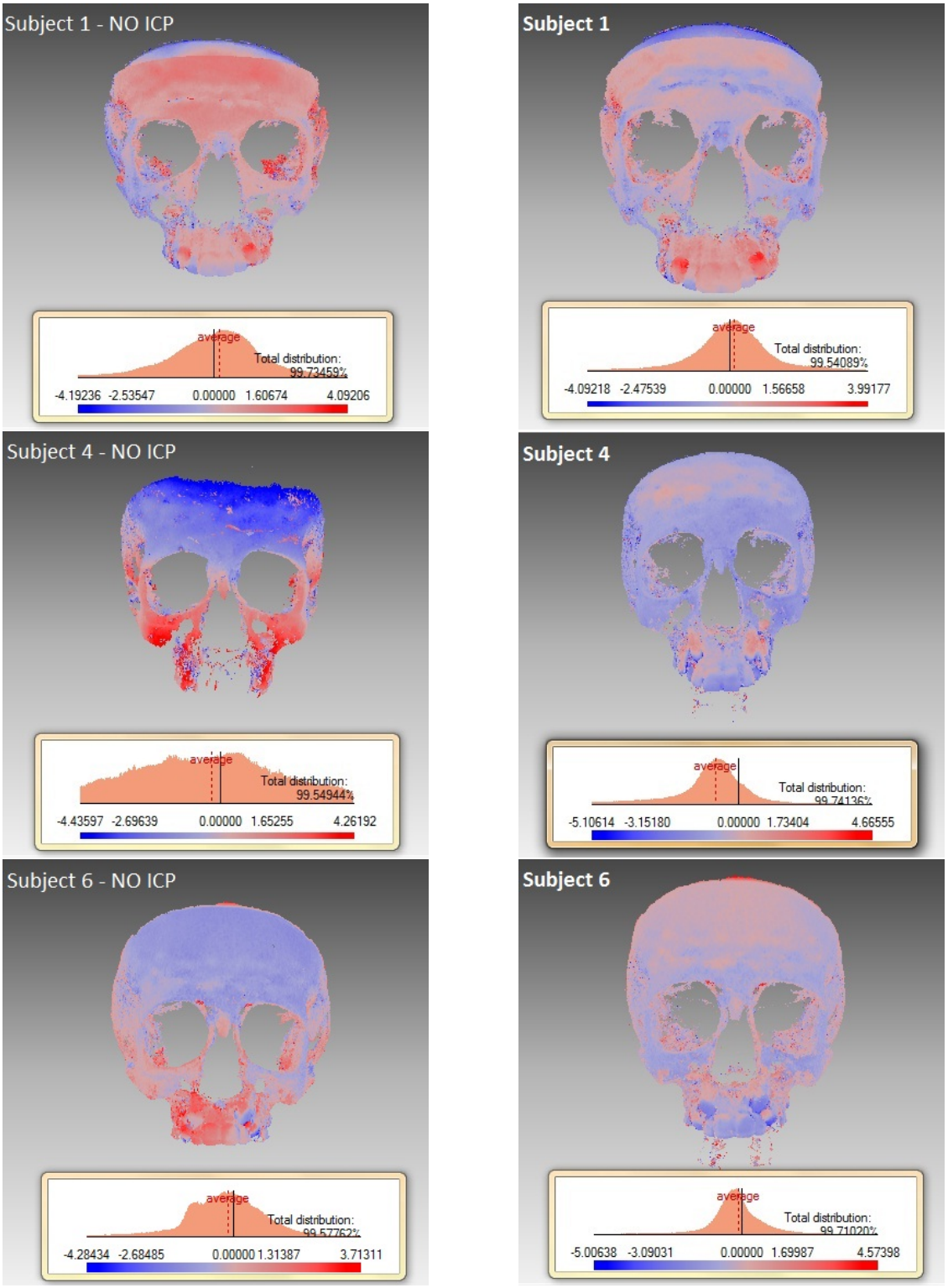

Figure 5.12: Registration results of multi-temporal data of CBCT between T_1 and T_2, for treated subjects. The left pictures show the results of the landmark-based registration algorithm, and the right pictures show the effect of the ICP algorithm on them. The registration errors are more distributed around zero after applying the ICP algorithm, which means that the registration between the corresponding points have been improved.

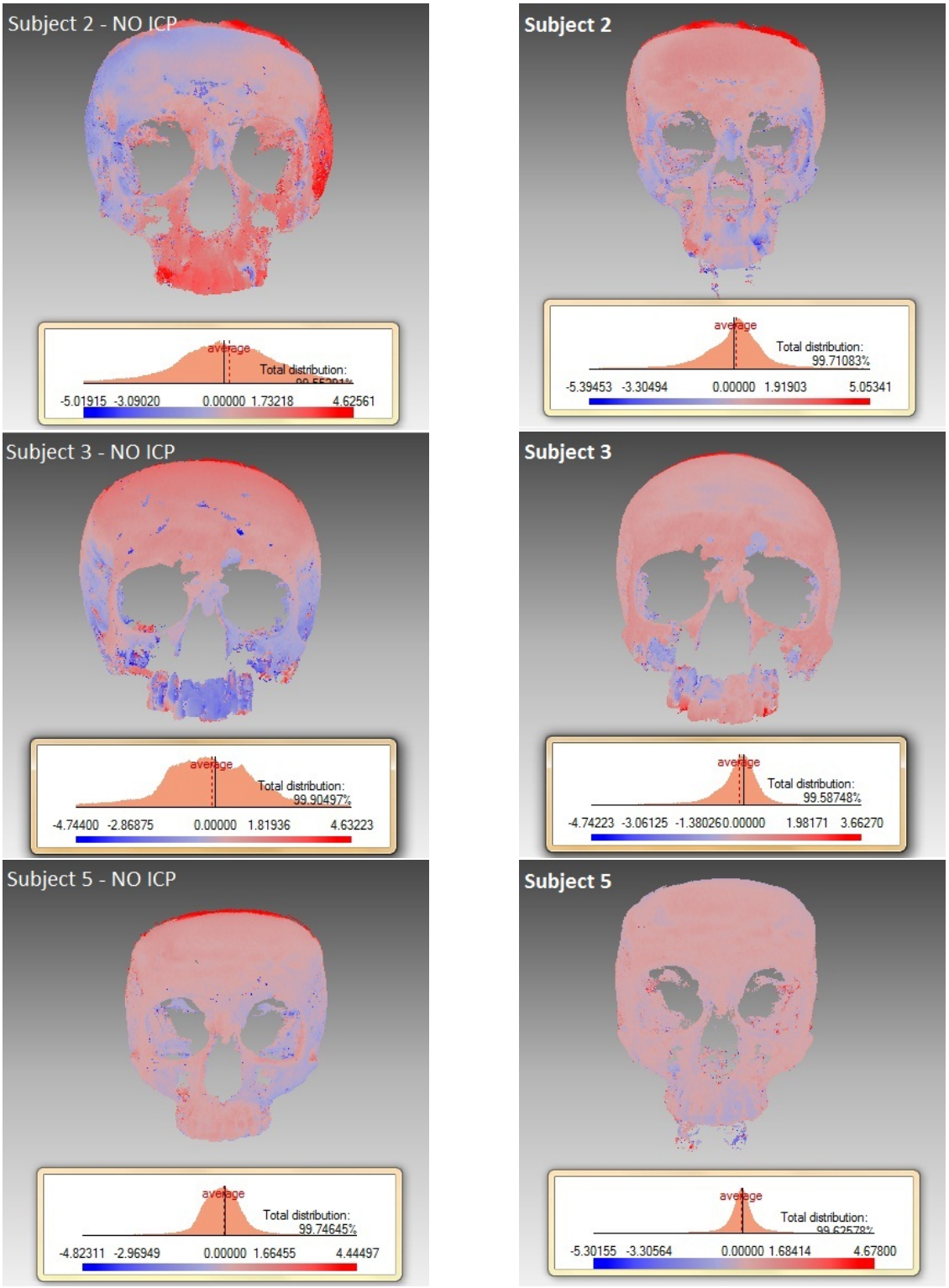

Figure 5.13: Registration results of multi-temporal data of CBCT between T_1 and T_2, for untreated subjects. The left pictures show the results of the landmark-based registration algorithm, and the right pictures show the effect of the ICP algorithm on them. The registration errors are more distributed around zero after applying the ICP algorithm, which means that the registration between the corresponding points have been improved.

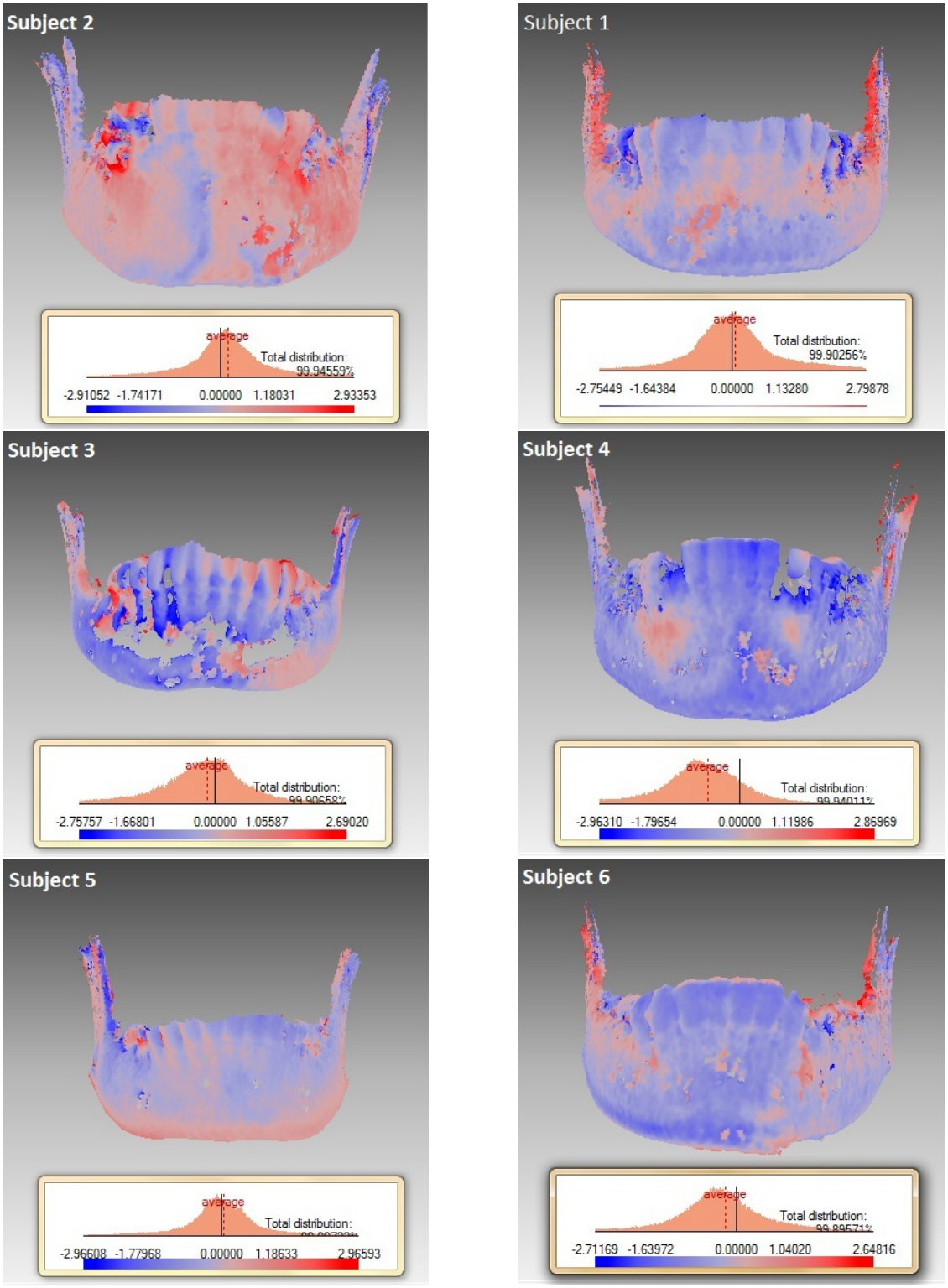

Figure 5.14: Results of registered mandibles between $T1$ and $T2$ using intrinsic landmark-based method. The left column shows the results for untreated subjects and the right column represents the procedure for treated ones. The dark colors represent larger registration errors (in mm) on the skulls, and the graphs show the distribution of signed deviations for the registration errors. As shown, the errors are distributed around zero, meaning that the registration procedure is not biased.

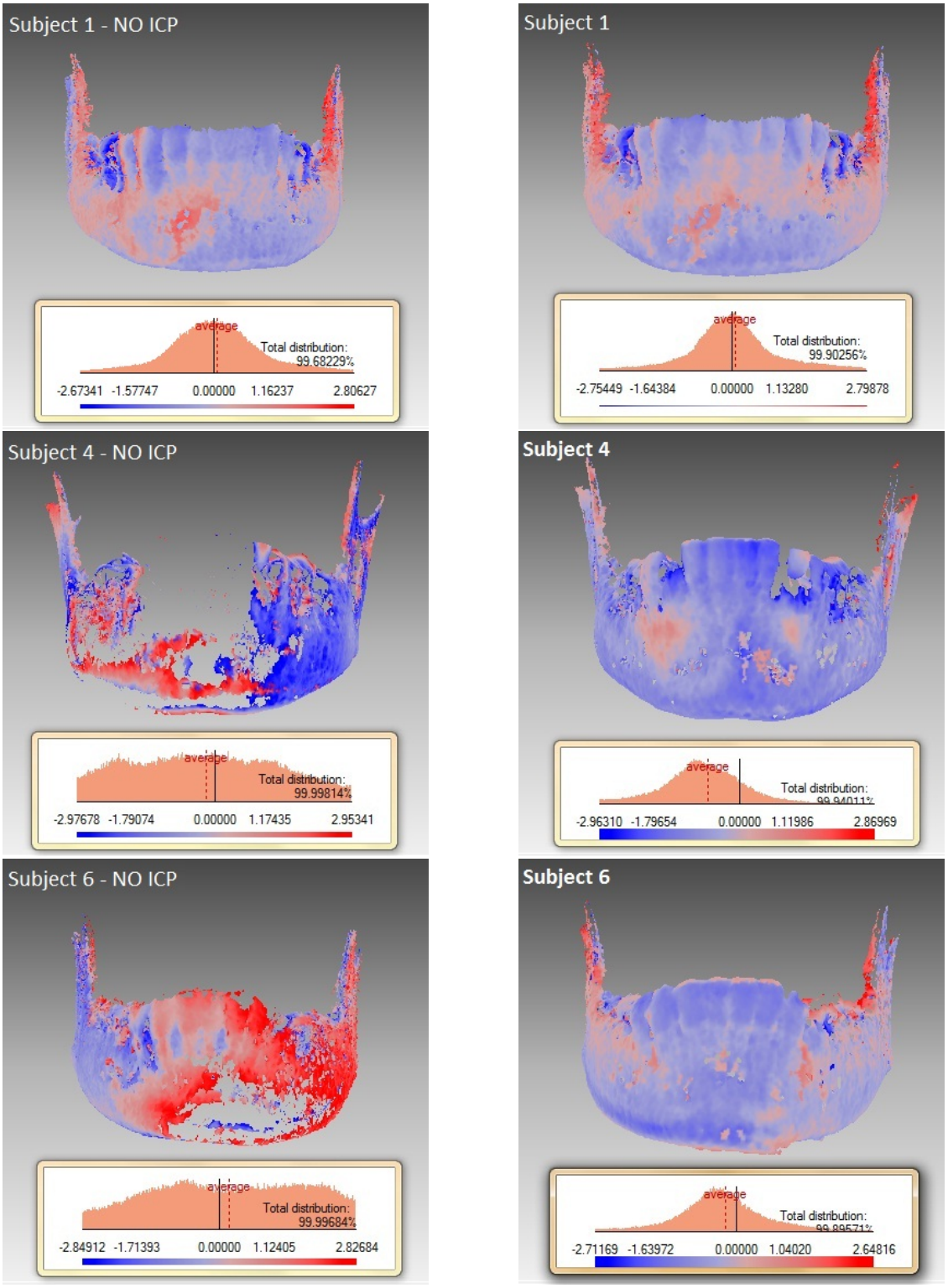

Figure 5.15: Registration results of multi-temporal data of CBCT between T_1 and T_2, for treated subjects. The left pictures show the results of the landmark-based registration algorithm, and the right pictures show the effect of the ICP algorithm on them. The registration errors are more distributed around zero after applying the ICP algorithm, which means that the registration between the corresponding points have been improved.

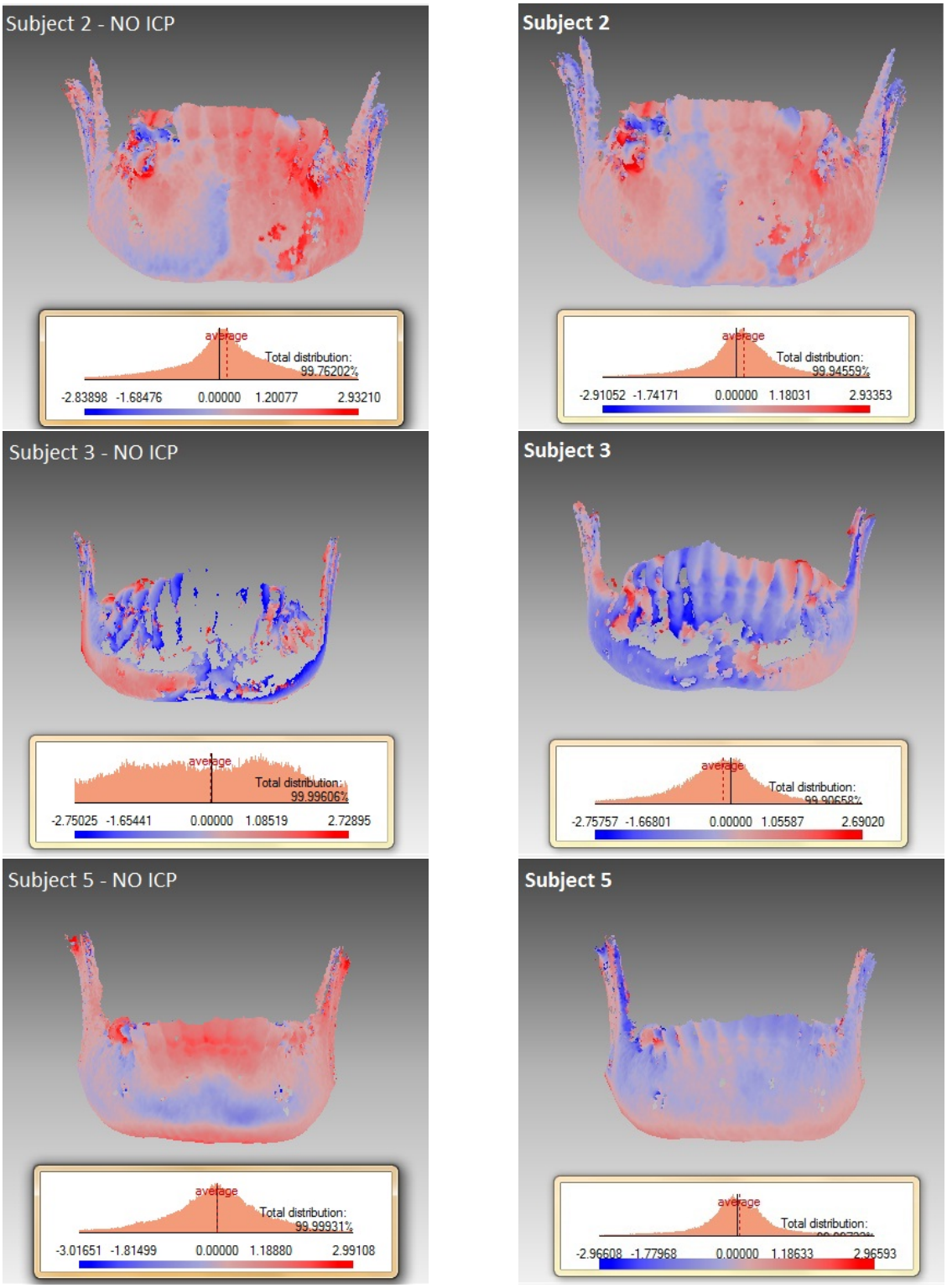

Figure 5.16: Registration results of multi-temporal data of CBCT between T_1 and T_2, for untreated subjects. The left pictures show the results of the landmark-based registration algorithm, and the right pictures show the effect of the ICP algorithm on them. The registration errors are more distributed around zero after applying the ICP algorithm, which means that the registration between the corresponding points have been improved.

5.4 Registration Validation

We used the signed distance as a measure to validate our proposed registration methodology. For each subject, we extracted the signed distance between the T_1 and T_2 skulls as well as those for T_1 and T_2 mandibles, and plotted the histograms of the measurements to visualize the error distributions. In our experiment, we expect our registration errors to follow a normal (Gaussian) distribution if there is no bias involved in the registration process, as any miss-registration data will create an error distribution that will not follow the Gaussian assumption. In this section, we are focusing on normal distributions, and the different tests that can be used to determine how likely it is that the error distributions can be modeled by a normal distribution.

5.4.1 Normal Distribution

A normal distribution, also known as Gaussian distribution, is a bell-shaped probability distribution with a single peak, which can be defined with the following probability density function (pdf):

$$f(x) = \frac{1}{\sigma\sqrt{2\pi}} e^{-\frac{1}{2}(\frac{x-\mu}{\sigma})^2}$$

where μ is the mean where the peak of the density occurs, and σ is the standard deviation which shows the spread of the distribution.

A very important property of normal distribution is the three-sigma or 68-95-99.7 rule. This rule states that in a normally distributed population, almost all values are within a $\mu \pm 3\sigma$ range. More specifically, this rule indicates that 68% of the values lie within a $\mu \pm \sigma$ range, 95% within a $\mu \pm 2\sigma$ range, and nearly all (99.7%) within a $\mu \pm 3\sigma$ range.

5.4.2 Skewness Measure

The first step before testing the normality of the error distributions is to calculate a skewness measure. Skewness is the measure of lack of symmetry of the distribution, and measures if the error data are distributed more to the right or to the left of

the mean. A perfect normal distribution is symmetric, and therefore the skewness measure is equal to zero. However, for experimental normal distributions which are not perfectly symmetric, a skewness measure less than or equal to 0.5 is considered symmetric. This measure is calculated as follows:

$$skewness = \frac{E(x-\mu)^3}{\sigma^3}$$

where μ is the mean of x, σ is the standard deviation of x, and E is the expected value.

5.4.3 Normality Tests

Two different tests are used to determine if the experimental distributions follow the normality assumption. A visual test consists of comparing the histograms of the signed distances with a normal curve. The graphical representation of distributions should be a bell-shaped curve with a single peak around the average μ centered in our case around zero. However, comparing other properties of a normal distribution is not possible visually. Therefore, a quantitative test such as the Chi-Square goodness-of-fit test is used after a visual inspection is successful.

In this thesis, we used the Chi-Square [56] to test the normality of our results. This test gets a vector data x as a sample of a data set, and estimates the mean and variance of the normal distribution from the signed error of each point. The null hypothesis that the error is a random sample from a normal distribution will be tested against the alternative hypothesis which is defined as the error is not normally distributed with the estimated mean and variance values.

H_0: The error distribution comes from a normal distribution.

H_a: The error does not come from a normal distribution.

Chi-Square test divides the sample data into N bins, and performs the following statistics:

$$\chi^2 = \sum_{i=1}^{N} \frac{(O_i - E_i)^2}{E_i} \tag{5.1}$$

where O_i is the observed frequency for bin i, and E_i is the expected frequency for bin i. Considering that cumulative distribution function (CDF) is the probability

that a variable X takes a value less than or equal to a specified value x:

$$CDF(\mu) = P[X \leq \mu] = \int_{-\infty}^{\mu} f(x)dx,$$

the expected frequency E_i for bin i would be calculated as follows:

$$E_i = S(CDF(U) - CDF(L))$$

where S is the sample size, U is the upper limit for bin i, and L is the lower limit for bin i.

Rejection Region

The null hypothesis will be rejected if

$$\chi^2 > \chi^2_{(\alpha,df)},$$

where α is the desired significance level, df is the degree of freedom calculated by $(N-1)$, and χ^2 is determined from Equation 5.1. The look-up table published by Fisher et. al in [20] shows χ^2 values versus P-values for different degrees of freedom. With the significance level $P = \alpha$, the value of $\chi^2_{(\alpha,df)}$ is extracted from an already existing table of χ^2 values.

If the sample comes from a normally distributed data, χ^2 would be smaller than $\chi^2_{(\alpha,df)}$, and the null hypothesis cannot be rejected at the significance level α. Otherwise, if the χ^2 is larger than $\chi^2_{(\alpha,df)}$, the null hypothesis can be rejected at significance level α. In this case, a P-value which shows the probability of observing the result, or one more extreme cases under the assumption that the null hypothesis is true, would also be returned. This value can be used for a better estimation of α in case the null hypothesis is rejected. A P-value of 0.05 or less is considered as statistically significant.

5.5 Registration Statistics

Our experiments on six subjects contain two registration results:

1. Skull Registration

2. Mandible Registration

For each subject, we extracted the signed distances between T_1 and T_2 surfaces for both the skull and the mandible registration results. Due to the hardware limitations, we extracted 1% of the signed distances as sample data from the Rapidform software to perform evaluation tests.

Prior to performing different statistical tests on the sampled data, we removed outliers from both the skull and the mandible data which did not fall inside the range of $2.5 * \sigma(dataset)$. Moreover, a tighter threshold of $1.5 * \sigma(dataset)$ was used on the skull data of subject5 and subject6. We propose that the presence of the outliers is due to the following reasons:

1. *The effect of the treatment on the treated patients*: The orthodontic changes on patients' teeth has influenced the measured distances from T_1 to T_2.

2. *Biological changes*: Biological changes such as teeth growth has affected the registration procedure. A big part of the calculated large deviations are due to the growing of canine teeth between the T_1 and T_2 scanning processes, especially for teenagers.

3. *Segmentation*: Extraction of skulls bone from the CT data taken at different points of time T_1 and T_2, even with the same parameters, results in different density of data-points that may be due to CT intensity calibration. This segmentation error can produce large outliers if the scanning parameters are not controlled.

In the rest of this section, the following statistical results will be represented,

1. Registration precision estimation,

2. Graphic representation of the distributions, and

3. Chi-square normality test.

Tables 5.1 and 5.2 show the mean, standard deviation and skewness measures of the signed errors in millimeter, for the skull and the mandible registrations, re-

Table 5.1: Information extracted from skull registrations regarding the signed distances (in mm) between corresponding points in T_1 and T_2.

UNTREATED	Subject2	Subject3	Subject5
Mean	0.1502	-0.0167	0.0144
Standard Deviation	0.5199	0.4752	0.2713
Skewness Measure	0.3006	0.0752	0.2441
TREATED	Subject1	Subject4	Subject6
Mean	0.1567	-0.4801	-0.0202
Standard Deviation	0.4895	0.6413	0.2705
Skewness Measure	0.132	-0.0081	0.0632

Table 5.2: Information extracted from mandible registrations regarding the signed distance (in mm) between corresponding points in T_1 and T_2.

UNTREATED	Subject2	Subject3	Subject5
Mean	0.2122	-0.0781	0.0700
Standard Deviation	0.5756	0.5954	0.5772
Skewness Measure	0.4440	0.0268	0.3598
TREATED	Subject1	Subject4	Subject6
Mean	0.0762	-0.4899	-0.1241
Standard Deviation	0.5571	0.5827	0.5416
Skewness Measure	0.2937	-0.1684	0.0752

spectively. As represented, the skewness measures of all the errors are in the range of [-0.5 , 0.5], hence making the error distributions approximately symmetric.

5.5.1 Registration Precision Estimation

The precision of the entire registration system is calculated by $\mu \pm \sigma$, where μ is the mean of the registration error, and σ is the standard error of our sample data. As shown in Table 5.3, all the registration precisions are smaller than 1.9mm reported in [46], and 1.5mm reported in [28] as the precision of CBCT devices.

5.5.2 Graphic Representation of the Distributions

For each subject, the distribution of signed errors was plotted by a histogram with 100 bins for the skulls and the mandibles. One can see in Figures 5.17 to 5.22 the signed error distributions for the skulls. Similarly, Figures 5.23 to 5.28 repre-

Table 5.3: Calculated registration precisions (in mm) for the skull and the mandible.

SKULL-TREATED	Subject1	Subject4	Subject6
Precision	0.1567±0.4895	-0.4801±0.6413	-0.0202±0.2705
SKULL-UNTREATED	Subject2	Subject3	Subject5
Precision	0.1502±0.5199	-0.0167±0.4752	0.0144±0.2713
MANDIBLE-TREATED	Subject1	Subject4	Subject6
Precision	0.0762±0.5571	-0.4899±0.5827	-0.1241±0.5416
MANDIBLE-UNTREATED	Subject2	Subject3	Subject5
Precision	0.2122±0.5756	-0.0781±0.5954	0.0700±0.5772

sent the signed error distributions for the mandibles. In all the figures, the normal distribution fitted on the error distributions are also represented.

From visual observations, one *cannot reject* the null hypothesis stating that the histograms are normally distributed. They are all bell-shaped symmetric histograms, with a single peak around their mean values. However, we need to know quantitatively how well the histograms are following a normal distribution, in order to certify that our registration technique is not biased. As mentioned previously, this can be tested by using a chi-square normality test on the error distributions.

5.5.3 Chi-Square Normality Test

Chi-Square normality test was used to test the normality of the error distributions on both the skull and the mandible data. The results of the test showed that with alpha probability level of 5%, one cannot reject the null hypothesis that our data follow a normal distribution. Moreover, the results of the zero-mean test using one-sample t-test on the skull and the mandible data show that except for two data sets (subject2 and subject4), this test could not reject the hypothesis that the our data is following a normal distribution with zero mean. Table 5.4 and Table 5.5 show the results of these two tests for skull and mandible error distributions.

Table 5.4: The results of Chi-Square normality test, and the zero-mean T-test on the error distrbutions of skull data. The second column shows the P value, the Chi-square value, and the degree of freedom for Chi-square normality test, and the third column shows the P value, the T value, and the degree of freedom for zero-mean T-Test.

SKULL	Chi-Square Normality Test	Zero-Mean T-Test
	P-Value, Chi-Square Value, DoF	P-Value, T-Value, DoF
Subject1	0.2772,6.3106,5	0.1704,1.3809,99
Subject2	0.6679,3.2081,5	REJECTED
Subject3	0.5936,3.6984,5	0.4278,-0.7962,99
Subject4	0.5894,3.7267,5	REJECTED
Subject5	0.4514,4.7166,5	0.8806,0.1506,99
Subject6	0.3675,5.4133,5	0.7952,-0.2603,99

Table 5.5: The results of Chi-Square normality test, and the zero-mean T-test on the error distrbutions of mandible data. The second column shows the P value, the Chi-square value, and the degree of freedom for Chi-square normality test, and the third column shows the P value, the T value, and the degree of freedom for zero-mean T-Test.

MANDIBLE	Chi-Square Normality Test	Zero-Mean T-Test
	P-Value, Chi-Square Value, DoF	P-Value, T-Value, DoF
Subject1	0.3135,7.0800,6	0.8668,0.1679,199
Subject2	0.1419,8.2721,5	REJECTED
Subject3	0.4595,6.7118,7	0.6815,-0.4111,199
Subject4	0.5308,5.1022,6	REJECTED
Subject5	0.5337,4.1097,5	0.8241,0.2225,199
Subject6	0.5828,3.7712,5	0.1552,1.4267,199

5.6 Summary

In this chapter, we first explained the data acquisition and pre-processing techniques used. Then the two phases of registration procedures were explained. In the first phase, we introduced a methodology for multi-modal registration of CBCT and 3dMD, and in the second phase we explained the multi-temporal registrations for the skulls and the mandibles.

Evaluating our registration results, we measured the signed distances between the corresponding points in images obtained at T_1 and T_2. We then tested the signed

distance errors with a Chi-Square goodness-of-fit test. The results of our normality tests showed that with the removal of the outliers, all the error data are following normal distributions which shows that our registration methodology is not biased and is reliable.

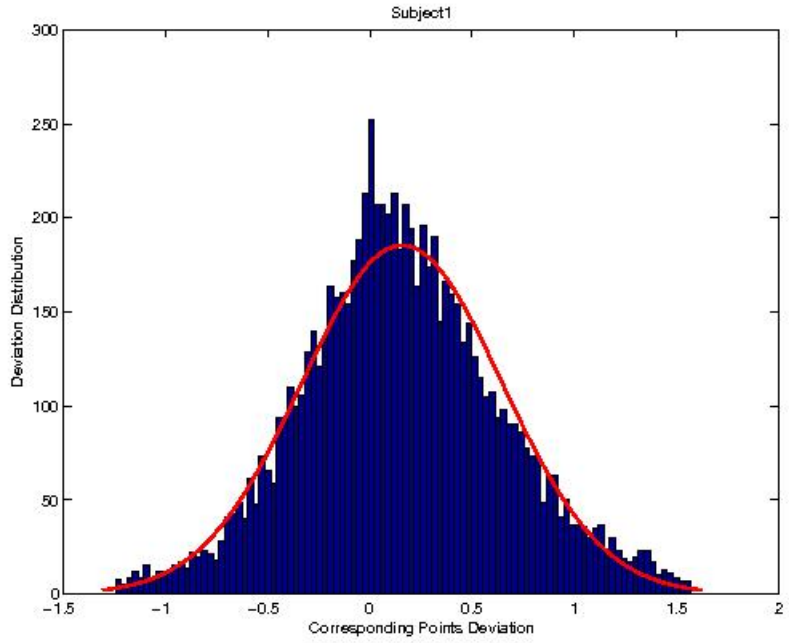

Figure 5.17: Distribution of signed registration errors (in mm) for Subject 1 - Skull. This error distribution is a normal distribution tested by Chi-Square normality test, and therefore indicates that the registration procedure is not biased.

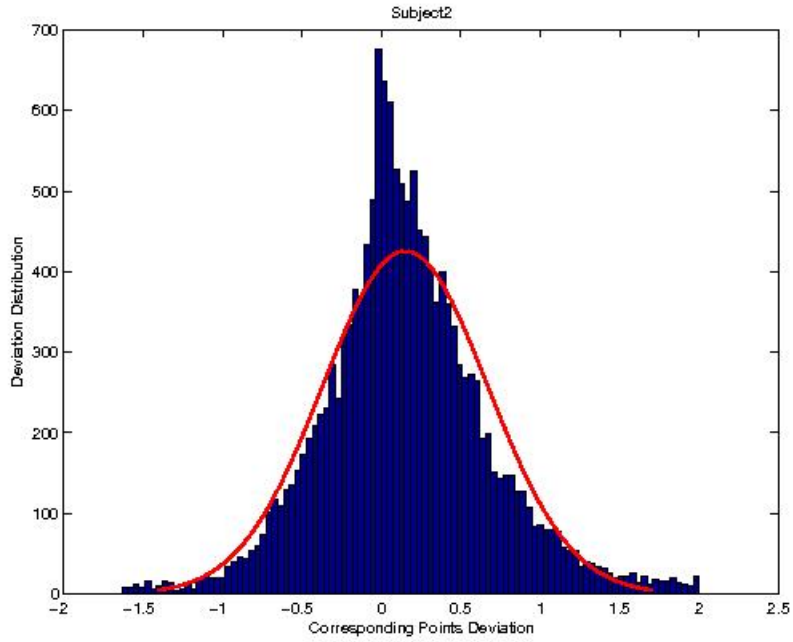

Figure 5.18: Distribution of signed registration errors (in mm) for Subject 2 - Skull. This error distribution is a normal distribution tested by Chi-Square normality test, and therefore indicates that the registration procedure is not biased.

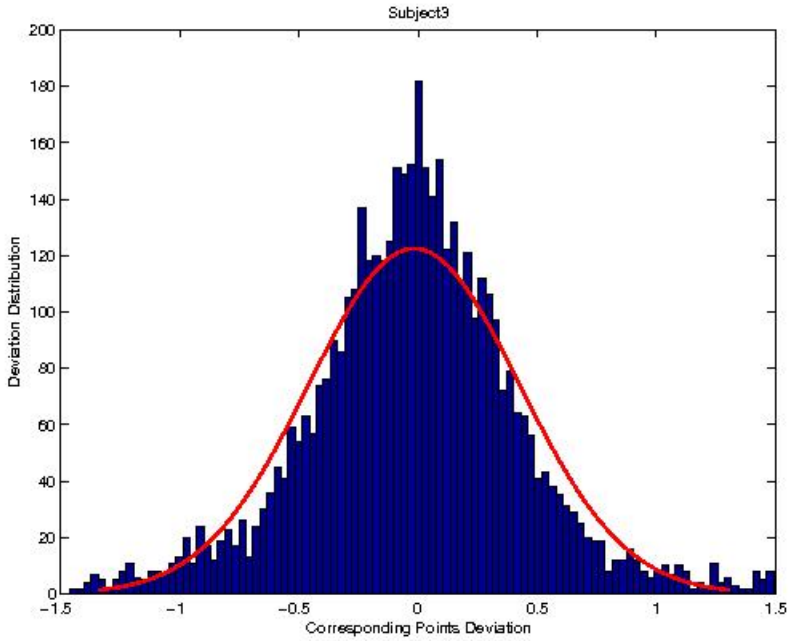

Figure 5.19: Distribution of signed registration errors (in mm) for Subject 3 - Skull. This error distribution is a normal distribution tested by Chi-Square normality test, and therefore indicates that the registration procedure is not biased.

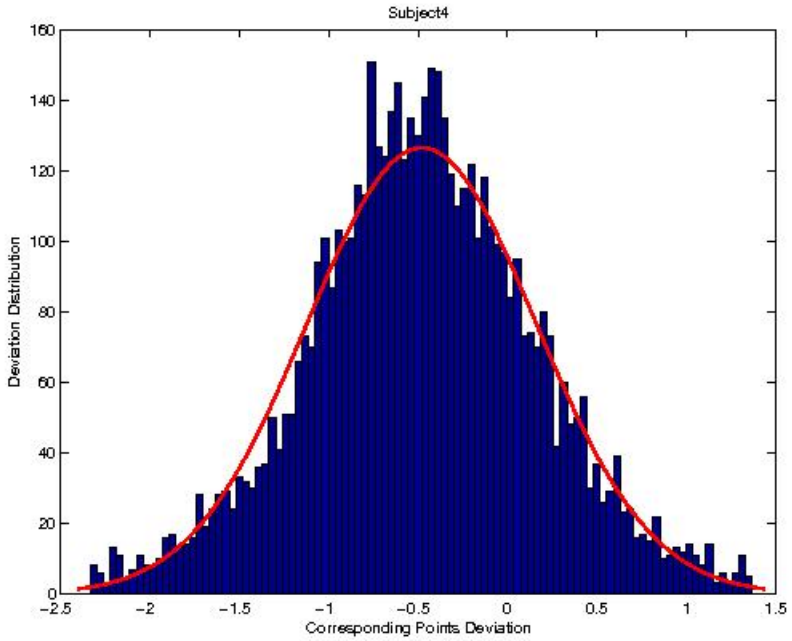

Figure 5.20: Distribution of signed registration errors (in mm) for Subject 4 - Skull. This error distribution is a normal distribution tested by Chi-Square normality test, and therefore indicates that the registration procedure is not biased.

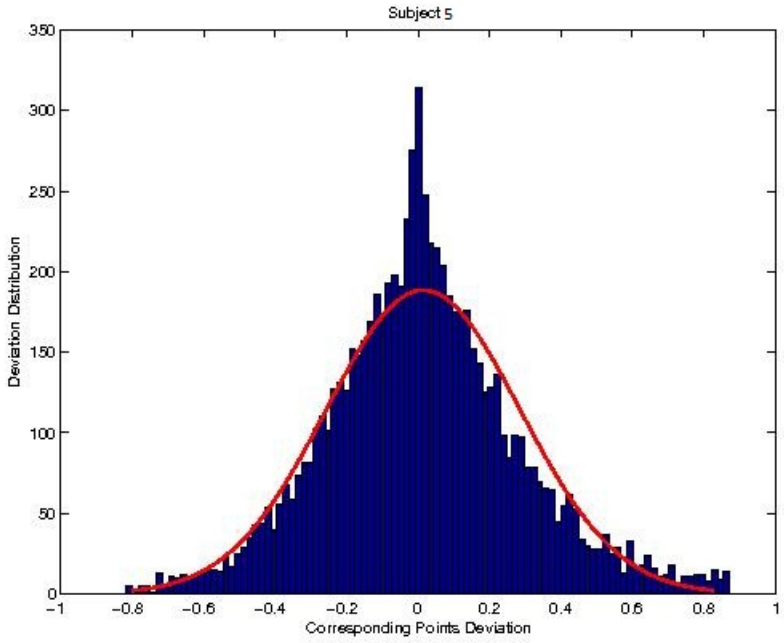

Figure 5.21: Distribution of signed registration errors (in mm) for Subject 5 - Skull. This error distribution is a normal distribution tested by Chi-Square normality test, and therefore indicates that the registration procedure is not biased.

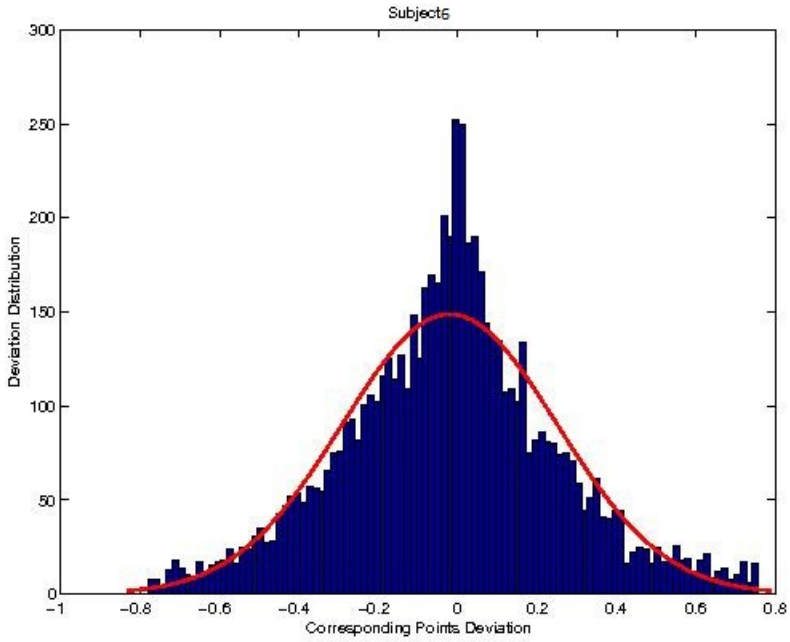

Figure 5.22: Distribution of signed registration errors (in mm) for Subject 6 - Skull. This error distribution is a normal distribution tested by Chi-Square normality test, and therefore indicates that the registration procedure is not biased.

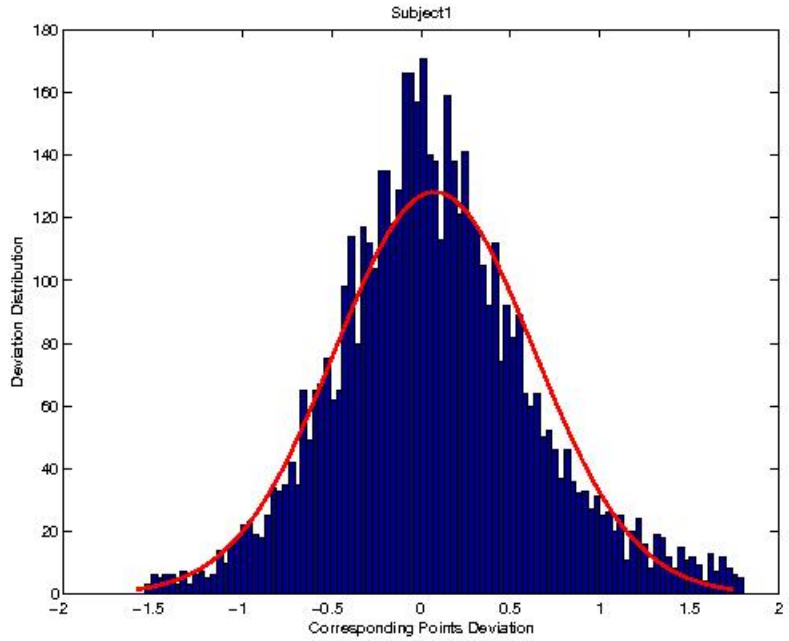

Figure 5.23: Distribution of signed registration errors (in mm) for Subject 1 - Mandible. This error distribution is a normal distribution tested by Chi-Square normality test, and therefore indicates that the registration procedure is not biased.

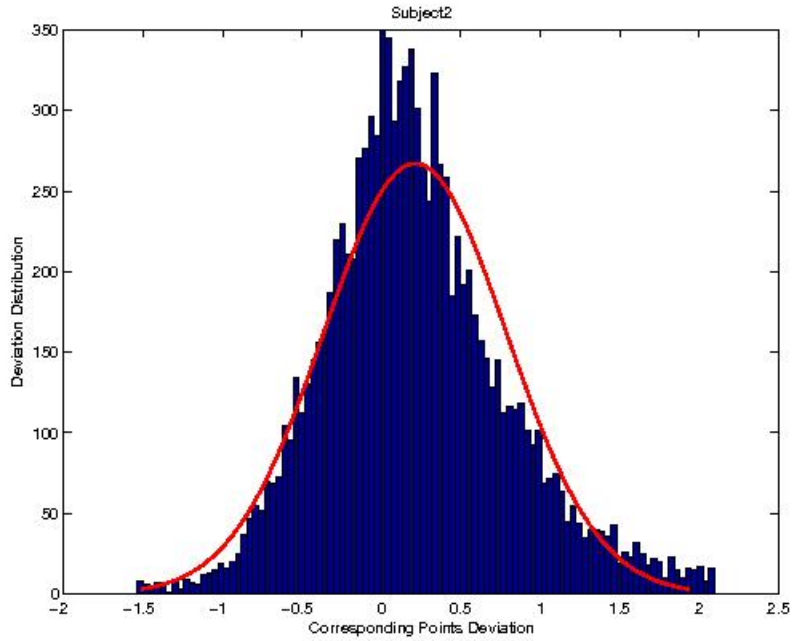

Figure 5.24: Distribution of signed registration errors (in mm) for Subject 2 - Mandible. This error distribution is a normal distribution tested by Chi-Square normality test, and therefore indicates that the registration procedure is not biased.

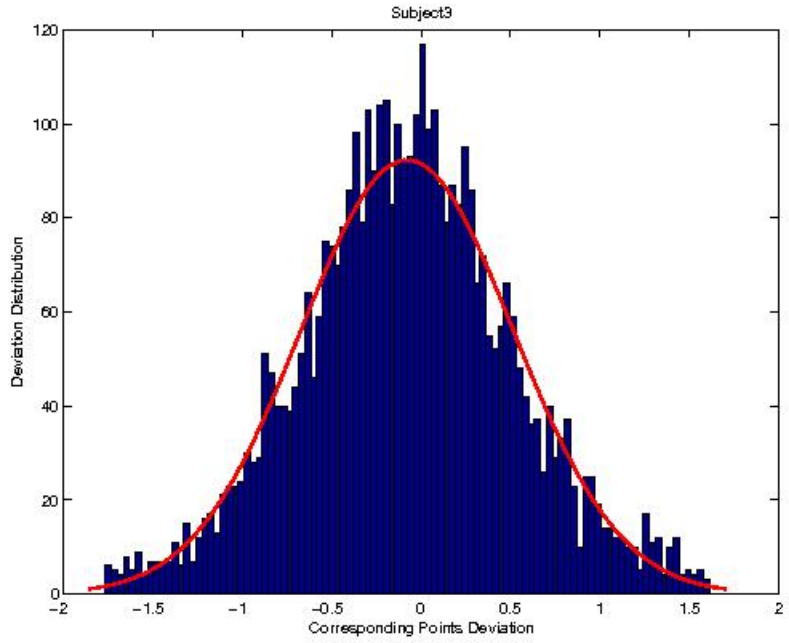

Figure 5.25: Distribution of signed registration errors (in mm) for Subject 3 - Mandible. This error distribution is a normal distribution tested by Chi-Square normality test, and therefore indicates that the registration procedure is not biased.

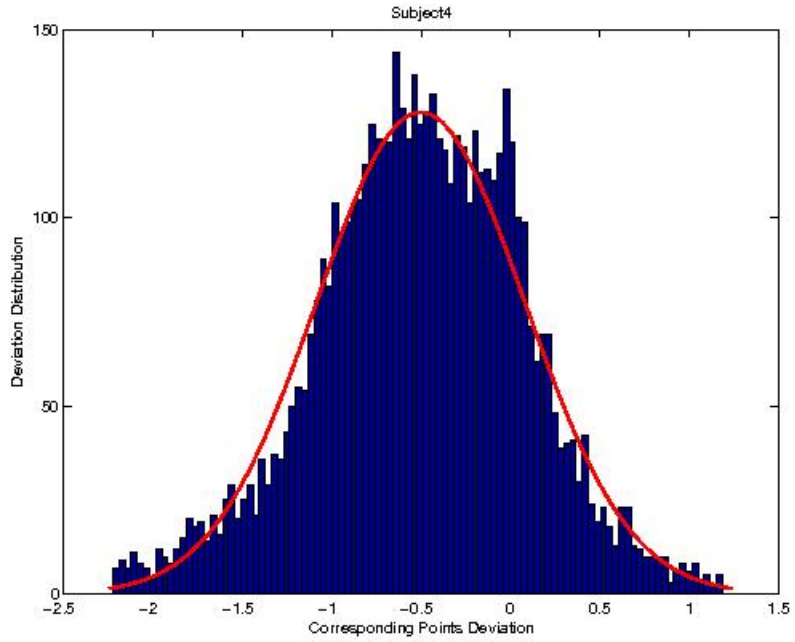

Figure 5.26: Distribution of signed registration errors (in mm) for Subject 4 - Mandible. This error distribution is a normal distribution tested by Chi-Square normality test, and therefore indicates that the registration procedure is not biased.

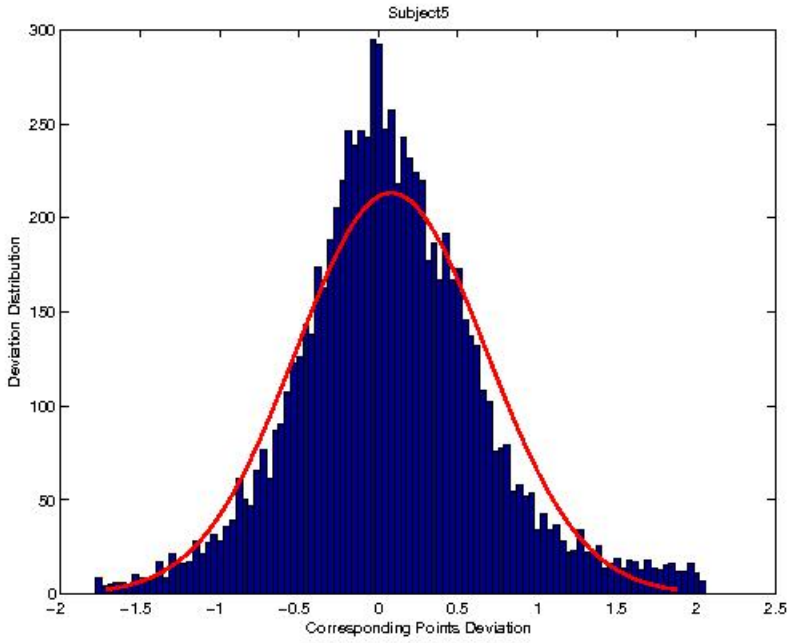

Figure 5.27: Distribution of signed registration errors (in mm) for Subject 5 - Mandible. This error distribution is a normal distribution tested by Chi-Square normality test, and therefore indicates that the registration procedure is not biased.

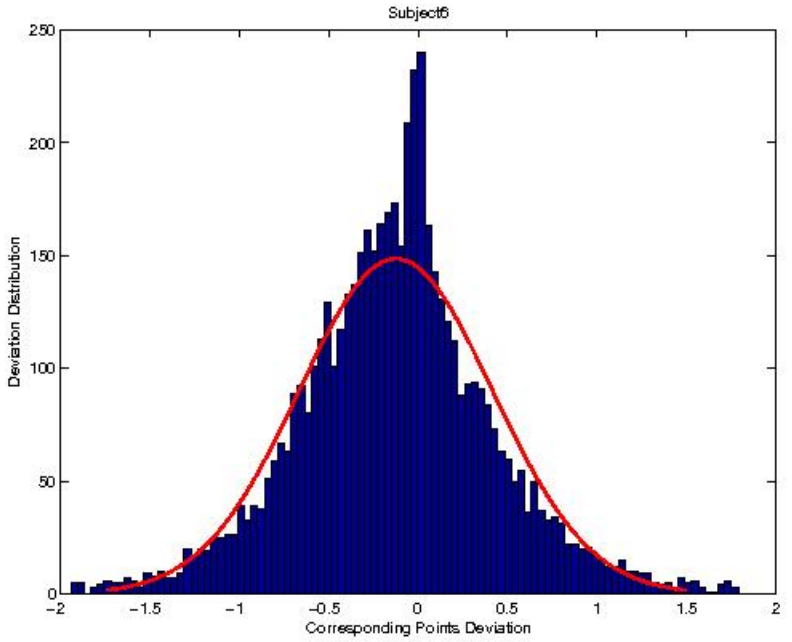

Figure 5.28: Distribution of signed registration errors (in mm) for Subject 6 - Mandible. This error distribution is a normal distribution tested by Chi-Square normality test, and therefore indicates that the registration procedure is not biased.

Chapter 6

Conclusion

Integrating multiple 3D imaging modalities in dentistry gives us the ability to reconstruct different tissue types, such as bone and skin, and to visualize 3D models of the patients. The information obtained from the reconstruction of different tissues in 3D before and after the treatments may help quantifying patient outcomes, which results in development of better treatments and objective surgical plannings.

In this thesis, we introduced a methodology for tracking bone and facial skin variations over a one-year period of time, in this case following an orthodontic treatment. Due to the fact that complementary information can be achieved from multiple modalities, CBCT and stereo-photogrammetry technologies are utilized to reconstruct bone and skin structures of the face. Six subjects, including three subjects experiencing a treatment and three untreated subjects, were chosen from an ongoing clinical trial, and undergone the data acquisition process at two different points of times (T_1 and T_2), within an 8 to 12 months period. During each imaging session, a headband with six titanium spheres glued to it was worn by the subjects.

A NewTom QR-DVT 9000 CBCT scanner was used to capture all the needed information for volumetric reconstruction of the skull and the teeth through only one rotation of the X-ray source and detector around the head. Once the scanning was performed, the data received by the detector was transmitted to a workstation where a 3D volumetric model of the skull was reconstructed by a backprojection algorithm implemented in the NewTom software.

A 3dMDface system mounted on top of the NewTom CBCT device was also used for skin texture and color acquisition just after the bone acquisition process

was done. By solving correspondence problem for the images captured from the four stereo-paired cameras, the corresponding points were detected, and a complicated triangulation algorithm was used to reconstruct the 3D model of the face. This system was then used to reproject the surface skin color captured by two high resolution cameras into the 3D model.

Comparing 3D models of the skull with the skin captured at one point of time gives us the ability to analyze the effects of bone variations on the skin structures. Moreover, comparing skull and skin variations before and after the treatments may help physicians to evaluate and plan for different treatments. As a consequence, a registration procedure is needed in order to overlay 3D skin over 3D skull models at each time and between visits, before and after the treatments.

Our proposed tracking system consisted of a two-phase registration procedure. In the first phase, we extracted from both modalities extrinsic landmarks which were put on the subjects' forehead during the imaging sessions, and registered them using a 3D rigid registration algorithm. The two geometric models (skull and face) were then registered in the same coordinate systems and saved as a unique polygonal shell that was used as one entity. As a result of this registration methodology, one can analyze the effects of bone treatments on the facial soft tissue.

In the second phase of registration, we took advantage of intrinsic landmarks on the skull geometry at times T_1 and T_2 to apply an automatic, robust registration algorithm. The skeletal anatomical landmarks were chosen among those which could be easily identifiable, and did not theoretically change or grow during the interval T_1 to T_2. In this way, by applying an intrinsic landmark-based registration followed by an Iterative Closest Points (ICP) algorithm, the skull data from time T_1 were registered on the skull data of time T_2, and comparisons among them were performed.

Since the mandibles can move independently to the upper-skulls and therefore should be registered separately, the same registration procedure with specific intrinsic landmarks was performed on the mandibles after they were segmented from the upper skull. Once the intrinsic landmark-based methodology was applied on the T_1 and T_2 datasets, the ICP algorithm was utilized to optimize the registration results.

Our registration methodology is shown to capture tissue variations accurately, with 95% of significance, for a few subjects and over a long period of time. The results of our registrations show that all of the measured errors stay within the CBCT device precision. Moreover, the registration errors for both mandible and skull data have been demonstrated to follow normal distributions with 95% significance, which shows that there is no bias regarding our registration methodology.

6.1 Future Work

Due to the relative high accuracy obtained from this methodology, it can be employed by dentists and physicians for tracking treatment results. However, a main source of outliers in our registration methodology, specially in the case of skulls, is caused by segmentation. Investigating the effects of different iso-surface values in Marching Cubes algorithm might result in finding the optimized value for registration. Additionally, developing an automatic process for the segmentation of mandibles, as well as automation of anatomical landmark detection might help reducing the outliers, and therefore improves the registration results.

Performing polygon morphing algorithms on soft tissue, bone and teeth data separately, and reconstructing polygonal models between patients' visits will help physicians to investigate the effects of treatments. Also, since 3dMD systems use light projection technique to find the corresponding point in stereo images, the colors captured by this device is different from the true colors. By developing a color calibration methodology, one would be able to extract the true color information from a photogrammetry system. Adding color information to morphing techniques will help find the color variations between times, and as a consequence, develop a complete track of the patients.

Bibliography

[1] 3dMD Incorporation. www.3dMD.com.

[2] A. Afsar, D.A. Haas, P.E. Rossouw, and R.E. Wood. Radiographic localization of mandibular anesthesia landmarks* 1. *Oral Surgery, Oral Medicine, Oral Pathology, Oral Radiology, and Endodontology*, 86(2):234–241, 1998.

[3] K. Aldridge, S.A. Boyadjiev, G.T. Capone, V.B. DeLeon, and J.T. Richtsmeier. Precision and error of three-dimensional phenotypic measures acquired from 3dMD photogrammetric images. *American Journal of Medical Genetics Part A*, 138(3):247–253, 2005.

[4] D.M Almog, J. LaMar, F.R. LaMar, and F. LaMar. Cone beam computerized tomography-based dental imaging for implant planning and surgical guidance, Part 1: Single implant in the mandibular molar region. *Journal of Oral Implantology*, 32(2):77–81, 2006.

[5] H. Azhari, R.R. Edelman, and D. Townsend. Multimodal Imaging and hybrid scanners. *Journal of Oral and Maxillodental Surgery*, 62(12):1497–1504, 2004.

[6] W.C.S. BDS and D. ABOMR. Cone beam computed tomography: A paradigm shift for clinical dentistry.

[7] G. Bebis. The correspondence problem: http://www.cse.unr.edu/ bebis/CS791E/Notes/StereoCorrespondenceProblem.pdf.

[8] P.J. Besl and N.D. McKay. A method for registration of 3-D shapes. *IEEE Transactions on pattern analysis and machine intelligence*, pages 239–256, 1992.

[9] P. Boulanger, C. Flores-Mir, JF Ramirez, E. Mesa, and JW Branch. Long term three dimensional tracking of orthodontic patients using registered cone beam CT and photogrammetry. *Conference proceedings:... Annual International Conference of the IEEE Engineering in Medicine and Biology Society. IEEE Engineering in Medicine and Biology Society. Conference*, 1:3525, 2009.

[10] M. Bro-Nielsen, C. Gramkow, and S. Kreiborg. Non-rigid image registration using bone growth model. In *CVRMed-MRCAS'97*, pages 1–12. Springer, 1997.

[11] LHS Cevidanes, LJ Bailey, GR Tucker Jr, MA Styner, A. Mol, CL Phillips, WR Proffit, and T. Turvey. Superimposition of 3D cone-beam CT models of orthognathic surgery patients. *Dentomaxillofacial Radiology*, 34(6):369, 2005.

[12] D. Chetverikov, D. Stepanov, and P. Krsek. Robust Euclidean alignment of 3D point set: the trimmed iterative closest point algorithm. *Image and Vision Computing*, 23(3):299–309, 2005.

[13] G.E. Christensen, S.C. Joshi, and M.I. Miller. Volumetric Transformation of brain anatomy. *IEEE Transaction on Medical Imaging*, 16(6):864–877, 1997.

[14] H. Chui and A. Rangarajan. A new point matching algorithm for non-rigid registration. *Computer Vision and Image Understanding*, 89(2-3):114–141, 2003.

[15] TJ Coward, BJJ Scott, RM Watson, and R. Richards. Laser scanning of the ear identifying the shape and position in subjects with normal facial symmetry. *International journal of oral and maxillofacial surgery*, 29(1):18–23, 2000.

[16] B. Erem and N. Dedual. Surface Construction Analysis using Marching Cubes. *Northeastern University, Boston. Kan laddas hem från: http://www. ndedual. com/wp-content/uploads/marchingcubes. pdf Senast bes "okt*, pages 08–12, 2009.

[17] E. Ezra, M. Sharir, and A. Eftar. On the ICP algorithm. In *Proceedings of the twenty-second annual symposium on computational geometry*, page 104. ACM, 2006.

[18] L.G. Farkas. *Anthropometry of the Head and Face*. Raven Pr, 1994.

[19] L. Fieten, K. Schmieder, M. Engelhardt, L. Pasalic, K. Radermacher, and S. Heger. Fast and accurate registration of cranial CT images with A-mode ultrasound. *International journal of computer assisted radiology and surgery*, 4(3):225–237, 2009.

[20] A. Fisher and F. Yates. *Statistical tables for biological, agricultural and medical research*. Longman Group United Kingdom, 1995.

[21] Alessandro Gherardi. *A skin surface characterization system based on capacitive image analysis*. PhD thesis, UNIVERSITA DI BOLOGNA, 2007.

[22] J.R. Gwilliam, S.J. Cunningham, and T. Hutton. Reproducibility of sof tissue landmarks on three-dimensional facial scans. *The European Journal of Orthodontics*, 28(5):408, 2006.

[23] TN. Hangartner. Thresholding technique for accurate analysis of density and geometry in QCT, pQCR and CT images. *J. Musculoskelet Neuronal Interact*, 7(1):9–16, 2007.

[24] W.E. Harrell Jr. Limitations of Two-Dimensional Cephalometric Analysis in Orthodontic Diagnosis and Treatment Planning: The need for Three-dimensional Diagnosis.

[25] W.E. Harrell Jr. Three-dimensional diagnosis & treatment planning: The use of 3D facial imaging and 3D cone beam CT in orthodontics and dentistry. *Austral Asian Dent Pract J*, 2007.

[26] C.L. Heike, K. Upson, E. Stuhaug, and S.M. Weinberg. 3D digital stereophotogrammetry: a practical guide to facial image acquisition. *Head and Face Medicine*, 6:18, 2010.

[27] C.F. Hildebolt and M.W. Vannier. Three-dimensional measurement accuracy of skull surface landmarks. *American Journal of Physical Anthropology*, 76(4):497–503, 1988.

[28] R.B. Howe. First molar radicular bone near the maxillary sinus: a comparison of CBCT analysis and gross anatomic dissection for small bony measurement. *Oral Surgery, Oral Medicine, Oral Pathology, Oral Radiology, and Endodontology*, 108(2):264–269, 2009.

[29] WW Howells. Criteria for selection of osteometric dimensions. *American journal of physical anthropology*, 30(3):451–457, 2005.

[30] Teknogem Incorporation. www.teknogem.com.

[31] CH Kau, A. Cronin, P. Durning, AI Zhurov, A. Sandham, and S. Richmond. A new method for the 3D measurement of postoperative swelling following orthognathic surgery. *Orthodontics & Craniofacial Research*, 9(1):31–37, 2006.

[32] CH Kau, S. Richmond, A. Incrapera, J. English, and JJ Xia. Three-dimensional surface acquisition systems for the study of facial morphology and their application to maxillofacial surgery. *The international journal of medical robotics+ computer assisted surgery: MRCAS*, 3(2):97, 2007.

[33] CH Kau, S. Richmond, JM Palomo, and MG Hans. Current Products and Practice: Three-dimensional cone beam computerized tomography in orthodontics. *Journal of orthodontics*, 32(4):282, 2005.

[34] C.H. Kau, A. Zhurov, S. Richmond, R. Bibb, A. Sugar, J. Knox, and F. Hartles. The 3-dimensional construction of the average 11-year-old child face: a clinical evaluation and application. *Journal of Oral and Maxillofacial Surgery*, 64(7):1086–1092, 2006.

[35] BS Khambay, J.C. Nebel, J. Bowman, F. Walker, D.M. Hadley, and AF Ayoub. 3D stereophotogrammetric image superimposition onto 3D CT scan images: the future of orthognathic surgery. A pilot study. *International Journal of Adult Orthodontics and Orthognathic Surgery*, 17(4):331–341, 2002.

[36] Y. Kitaaki, H. Okuda, H. Kage, and K. Sumi. High speed 3-D registration using GPU. *SICE Annual Conference*, pages 3055–3059, 2008.

[37] C. Lane and W. Harrel Jr. Completing the 3-dimensional picture. *Americal Journal of Orthodontics and Dentofacial Orthopedics*, 133(4):612–620, 2008.

[38] CA Lascala, J. Panella, and MM Marques. Analysis of the accuracy of linear measurements obtained by cone beam computed tomography (CBCT-NewTom). *Dentomaxillofacial Radiology*, 33(5):291, 2004.

[39] I. Lee. Survey of Isosurface Extraction and Surface Reconstruction.

[40] W.E. Lorensen and H.E. Cline. Marching cubes: A high resolution 3D surface construction algorithm. In *Proceedings of the 14th annual conference on Computer graphics and interactive techniques*, page 169. ACM, 1987.

[41] J. Luck, C. Little, and W. Hoff. Registration of range data using a hybrid simulated annealing and iterative closest point algorithm. *IEEE International Conference on Robotics and Automation*, 4:3739–3744, 2000.

[42] James Mah. X-ray imaging and oral healthcare. 2006.

[43] JB Maintz and M.A. Viergever. A survey of medical image registration. *Medical image analysis*, 2(1):1–36, 1998.

[44] Z. Majid, A.K. Chong, and H. Setan. Important considerations for craniofacial mapping using laser scanners. *The Photogrammetric Record*, 22(120):290–308, 2007.

[45] M. Mancas, B. Gosselin, and B. Macq. Segmentation using a region-growing thresholding. *Proc. SPIE*, 5672:388–398, 2005.

[46] B.A. Moerenhout, F. Gelaude, GR Swennen, J.W. Casselman, J. Van Der Sloten, and M.Y. Mommaerts. Accuracy and repeatability of cone-beam computed tomography (CBCT) measurements used in the determination of facial indices in the laboratory setup. *Journal of cranio-maxillo-facial surgery: official publication of the European Association for Cranio-Maxillo-Facial Surgery*, 37(1):18, 2009.

[47] A. Nestor and M.J. Tarr. Gender recognition of human faces using color. *Psychological Science*, 19(12):1242, 2008.

[48] T. Ogawa, R. Enciso, A. Memon, J.K Mah, and G.T. Clark. Evaluation of 3D airwau imaging of obstructive sleep apnea with cone-beam computed tomography. *Studies in Health Technology and Infomatics*, 111:365–368, 2005.

[49] S.M. Paul, A.P. Chamberlin, C. Hatt, A.V. Nayak, and J.V. Danoff. Reliability, validity, and precision of an active stereophotogrammetry system for three-dimensional evaluation of the human torso. *Medical Engineering and Physics*, 31(10):1337–1342, 2009.

[50] D.R. Periago, W.C. Scarfe, M. Moshiri, J.P. Scheetz, A.M. Silveira, and A.G. Farman. Linear accuracy and reliability of cone beam CT derived 3-dimensional images constructed using an orthodontic volumetric rendering program. *Journal Information*, 78(3), 2008.

[51] JM Plooij, GRJ Swennen, FA Rangel, TJJ Maal, FAC Schutyser, EM Bronkhorst, AM Kuijpers-Jagtman, and SJ Bergé. Evaluation of reproducibility and reliability of 3D soft tissue analysis using 3D stereophotogrammetry. *International journal of oral and maxillofacial surgery*, 38(3):267–273, 2009.

[52] S. Rusinkiewicz and M. Levoy. Efficient variants of the ICP algorithm. In *3dim*, page 145. Published by the IEEE Computer Society, 2001.

[53] W.C. Scarfe and A.G. Farman. What is cone-beam CT and how does it work? *Dental Clinics of North America*, 52(4):707–730, 2008.

[54] W.C. Scarfe, A.G. Farman, and P. Sukovic. Clinical applications of cone-beam computed tomography in dental practice. *Journal-Canadian Dental Association*, 72(1):75, 2006.

[55] D.A. Simon. *Fast and accurate shape-based registration*. PhD thesis, Carnegie Mellon University, 1996.

[56] G. Snedecor and W. Cochran. *Statistical Methods*. Iowa State University Press, 1967.

[57] SA Stratemann, JC Huang, K. Maki, AJ Miller, and DC Hatcher. Comparison of cone beam computed tomography imaging with physical measures. *Dentomaxillofacial Radiology*, 37(2):80, 2008.

[58] P. Suetens. *Fundamentals of medical imaging*. Cambridge Univ Pr, 2009.

[59] P. Sukovic. Cone beam computed tomography in craniofacial imaging. *Orthodontics & Craniofacial Research*, 6(s1):31–36, 2003.

[60] P. Vanezis, M. Vanezis, G. McCombe, and T. Niblett. Facial reconstruction using 3-D computer graphics. *Forensic Science International*, 108(2):81–95, 2000.

[61] S.C. White and M.J. Pharoah. The evolution and application of dental maxillofacial imaging modalities. *Dental Clinics of North America*, 52(4):689–705, 2008.

[62] F.L.E. Williams and J.T. Richtsmeier. Comparison of mandibular landmarks from computed tomography and 3D digitizer data. *Clinical Anatomy*, 16(6):494–500, 2003.

[63] J.Y. Wong, A.K. Oh, E. Ohta, A.T. Hunt, G.F. Rogers, J.B. Mulliken, and C.K. Deutsch. Validity and reliability of craniofacial anthropometric measurement of 3D digital photogrammetric images. *The Cleft Palate-Craniofacial Journal*, 45(3):232–239, 2008.